gebiology

Geobiology (2016), **14**, 105–128 DOI: 10.1111/gbi.12163

Carbon and sulfur isotopic signatures of ancient life and environment at the microbial scale: Neoarchean shales and carbonates

K. H. WILLIFORD,[1,2,3] T. USHIKUBO,[1,2,*] K. LEPOT,[1,2,†] K. KITAJIMA,[1,2] C. HALLMANN,[4,‡] M. J. SPICUZZA,[1,2] R. KOZDON,[1,2,§] J. L. EIGENBRODE,[5] R. E. SUMMONS[2,4] AND J. W. VALLEY[1,2]

[1]*Department of Geoscience, University of Wisconsin, Madison, WI, USA*
[2]*NASA Astrobiology Institute, University of Wisconsin, Madison, WI, USA*
[3]*Jet Propulsion Laboratory, California Institute of Technology, Pasadena, CA, USA*
[4]*Earth, Atmospheric and Planetary Science Department, Massachusetts Institute of Technology, Cambridge, MA, USA*
[5]*Planetary Environments Laboratory, NASA Goddard Space Flight Center, Greenbelt, MD, USA*

ABSTRACT

An approach to coordinated, spatially resolved, *in situ* carbon isotope analysis of organic matter and carbonate minerals, and sulfur three- and four-isotope analysis of pyrite with an unprecedented combination of spatial resolution, precision, and accuracy is described. Organic matter and pyrite from eleven rock samples of Neoarchean drill core express nearly the entire range of $\delta^{13}C$, $\delta^{34}S$, $\Delta^{33}S$, and $\Delta^{36}S$ known from the geologic record, commonly in correlation with morphology, mineralogy, and elemental composition. A new analytical approach (including a set of organic calibration standards) to account for a strong correlation between H/C and instrumental bias in SIMS $\delta^{13}C$ measurement of organic matter is identified. Small (2–3 μm) organic domains in carbonate matrices are analyzed with sub-permil accuracy and precision. Separate 20- to 50-μm domains of kerogen in a single ~0.5 cm^3 sample of the ~2.7 Ga Tumbiana Formation have $\delta^{13}C = -52.3 \pm 0.1‰$ and $-34.4 \pm 0.1‰$, likely preserving distinct signatures of methanotrophy and photoautotrophy. Pyrobitumen in the ~2.6 Ga Jeerinah Formation and the ~2.5 Ga Mount McRae Shale is systematically ^{13}C-enriched relative to co-occurring kerogen, and associations with uraniferous mineral grains suggest radiolytic alteration. A large range in sulfur isotopic compositions (including higher $\Delta^{33}S$ and more extreme spatial gradients in $\Delta^{33}S$ and $\Delta^{36}S$ than any previously reported) are observed in correlation with morphology and associated mineralogy. Changing systematics of $\delta^{34}S$, $\Delta^{33}S$, and $\Delta^{36}S$, previously investigated at the millimeter to centimeter scale using bulk analysis, are shown to occur at the micrometer scale of individual pyrite grains. These results support the emerging view that the dampened signature of mass-independent sulfur isotope fractionation (S-MIF) associated with the Mesoarchean continued into the early Neoarchean, and that the connections between methane and sulfur metabolism affected the production and preservation of S-MIF during the first half of the planet's history.

Received 17 May 2015; accepted 28 August 2015

Corresponding author: K. H. Williford. Tel.: +1 626 429 3528; fax: +1 818 393 4445;
e-mail: kenneth.williford@jpl.nasa.gov

*Present address: Kochi Institute for Core Sample Research, JAMSTEC, Nankoku, Kochi, Japan

†Present address: Laboratoire d'Océanologie et de Géosciences, Université de Lille, CNRS UMR8187, 59655 Villeneuve d'Ascq, France

‡Present address: Max Planck Institute for Biogeochemistry, Jena, Germany

§Present address: Lamont–Doherty Earth Observatory of Columbia University, Palisades, NY, USA

INTRODUCTION

The search for evidence of life and habitable environments in ancient sedimentary rocks is facilitated by the fact that elements essential to all known organisms (e.g., C, H, O, N, S) have multiple stable isotopes whose relative abundances change in characteristic ways when processed biologically. Isotopic fractionation results from both equilibrium and kinetic processes and can generate measurable differences in the compositions of metabolic substrates and products. Preservation of these metabolic substrates and products over million- and billion-year time scales, however, commonly includes their further transformation into relatively recalcitrant, complex mixtures of organic matter (kerogen and bitumen) or minerals (e.g., carbonates, quartz, oxides, sulfates, sulfides, etc.) through secondary (early diagenetic) processes that can impart additional, abiotic fractionations. After these secondary transformations, isotopic compositions of sedimentary organic matter and biominerals may be further altered by tertiary (late diagenetic) processes including metamorphism and metasomatism. Detection of stable isotopic signatures of life and environment, then, requires deconvolution of these post-metabolic, secondary, and tertiary alteration processes. The likelihood of biosignature alteration or destruction increases with increasing age, and it follows that any records of life and environment preserved in the most ancient rocks on Earth (and beyond) are likely to be sparse and ambiguous.

At the regional, outcrop, or drill-core scale, the extent to which biologically driven isotopic fractionation processes may be recorded in sediments can be assessed by geologic mapping, visual inspection of hand sample lithology, detailed petrographic analysis of selected samples, and bulk geochemistry. So-called 'bulk' or 'whole rock' stable isotope ratios of carbon ($\delta^{13}C$)[1] in organic matter and carbonates (e.g. Hayes, 1983, 1994; Eigenbrode & Freeman, 2006) and sulfur ($\delta^{34}S$) in sulfides and sulfates (e.g., Shen *et al.*, 2001, 2009) in powdered outcrop or drill-core samples provide important information about the evolution of biogeochemical cycles, including the presence and variable expression of particular metabolic pathways (e.g. photoautotrophy, methanotrophy, sulfate reduction). Paired carbon and oxygen isotope analysis in carbonates (e.g. Veizer *et al.*, 1990; Eigenbrode, 2004), including 'clumped' isotope patterns (Eiler, 2011) can provide important information about diagenetic effects that may obscure original biological signals. In rocks older than ~2.4 Ga, deviations in the relative abundances of the rare (^{33}S and ^{36}S) relative to the more common isotopes of sulfur (^{32}S and ^{34}S) from those expected due to purely mass-dependent processes ($\Delta^{33}S$ and $\Delta^{36}S$)[2] are thought to have been produced during UV disassociation of SO_2 and possible only in an anoxic atmosphere (Farquhar *et al.*, 2000). The preservation of such 'mass-independent' or 'non-mass-dependent' fractionation of sulfur isotopes (S-MIF) further requires that sulfur left the atmosphere as multiple, discreet molecular species (H_2SO_4 and S_8), and escaped homogenization due to a low concentration of sulfate in the oceans (Pavlov & Kasting, 2002; Ono *et al.*, 2003; Ono, 2008). Measurement of S-MIF has thus been used to constrain the timing of atmospheric oxygenation (Farquhar & Wing, 2003; Bekker *et al.*, 2004; Papineau *et al.*, 2007; Guo *et al.*, 2009; Williford *et al.*, 2011). Recent empirical and theoretical analysis of small deviations in biological fractionation effects between the individual sulfur isotopes (Johnston *et al.*, 2005; Johnston, 2011), as well as correlations between anomalously low bulk $\delta^{13}C_{org}$ values and small deviations in the ratio of $\Delta^{36}S$ to $\Delta^{33}S$ typical for Archean rocks (Thomazo *et al.*, 2009a,b, 2013; Zerkle *et al.*, 2012), suggests that information about atmosphere–biosphere interactions is uniquely accessible by coordinated carbon and sulfur four-isotope analysis (Ono *et al.*, 2006).

In this study, we build upon insights into the behavior of the Neoarchean (2.8–2.5 Ga) biosphere and atmosphere gained from coordinated bulk stable carbon and sulfur four-isotope analysis by developing and applying the techniques to detect these signals *in situ*, at the scale of the micro-organisms and microenvironments within which they were originally produced and preserved. Here, we report new methods for, and data from, carbon isotope analysis of kerogen, pyrobitumen, calcite, and dolomite, and sulfur three- and four-isotope analysis of pyrite using secondary-ion mass spectrometry (SIMS). These measurements are made in petrographic context provided by light and scanning-electron microscopy (SEM), as well as elemental analysis by energy-dispersive x-ray spectroscopy (EDS). Although this approach is resource intensive compared to traditional bulk measurements, and is therefore applied to a relatively small number of rock samples, the information density per sample is extraordinarily high and inaccessible by other means. The approach we outline here for spatially resolved, *in situ* stable carbon and sulfur isotope analysis provides unique insights into biosignature formation and alteration processes by revealing spatial heterogeneity and compositional patterns masked by bulk techniques.

[1] We report isotopic compositions in standard 'delta notation', for example $\delta^{13}C‰ = \left[\frac{\left(\frac{^{13}C}{^{12}C}\right)_{sample}}{\left(\frac{^{13}C}{^{12}C}\right)_{standard}} - 1\right] \times 1000$.

[2] $\Delta^{33}S = \delta^{33}S - 1000 \times \left[\left(1 + \frac{\delta^{34}S}{1000}\right)^{0.515} - 1\right]$;
$\Delta^{36}S = \delta^{36}S - 1000 \times \left[\left(1 + \frac{\delta^{34}S}{1000}\right)^{1.9} - 1\right]$

Archean organic geochemistry

Lipid biomarkers, including polycyclic terpenoids such as hopanes and steranes (the diagenetic products of bacterial and eukaryotic membrane lipid components, respectively), extracted from shales and carbonates of Neoarchean strata in the Pilbara Craton of Western Australia (WRL-1, RHDH2, and SV-1 cores), and sediments from the Transvaal Supergroup of the Kaapvaal Craton of South Africa (GKF and GKP cores) were proposed to record some of the oldest molecular evidence of life on Earth, including the oldest evidence for eukaryotes, and to indicate oxygenic photosynthesis hundreds of millions of years prior to initial atmospheric oxygenation (Brocks *et al.*, 1999, 2003a,b,c; Eigenbrode, 2004; Eigenbrode *et al.*, 2008; Waldbauer *et al.*, 2009).

These reports described the risks of false positives in the search for syngenetic Archean hydrocarbons, and the authors took great care to evaluate the possibilities for contamination that would have confounded their interpretations. Recently, as part of a wide-ranging collaborative effort to test whether the Archean biomarkers are indigenous and syngenetic using unprecedented contamination control measures during drilling and later sample handling, new drill cores intersecting sediments of the Fortescue and Hamersley Groups in the Pilbara have been obtained by the Agouron Institute Drilling Project. Analyses of the interior portions of these new core samples yielded hopane and sterane biomarker concentrations comparable to procedural blanks and negative controls, whereas analyses of exterior portions (and re-analyses of the formerly studied and correlative samples) yielded concentrations an order of magnitude higher, consistent with contamination (French *et al.*, 2015). This work demonstrates that alternative analytical approaches are needed to understand the biogeochemical records preserved in Archean organic matter.

SIMS analysis of Archean organic matter

The syngenicity of Neoarchean biomarkers was called into question earlier by a study that used spatially resolved, *in situ* $\delta^{13}C$ measurements of kerogen and pyrobitumen in samples of the Roy Hill Member of the Jeerinah Formation taken from the WRL-1, DDH 186, and FVG-1 drill cores. The authors argued on the basis of a 10–20‰ difference in $\delta^{13}C$ between the extracted hydrocarbons and less mobile, and relatively ^{13}C-depleted organic phases such as kerogen and pyrobitumen that the hydrocarbons must postdate peak metamorphism at ~2.2 Gyr ago (Rasmussen *et al.*, 2008). The measurements by Rasmussen *et al.* (2008) were made using a CAMECA NanoSIMS 50 (commonly called 'NanoSIMS' and distinct from the instrument used to collect data in this study) that rasters a beam of Cs^+ ions across a 25-μm^2 area on the surface of a sample. NanoSIMS excels at 50- to 100-nm scale elemental mapping (e.g. Oehler *et al.*, 2009). However, a number of factors such as quasi-simultaneous arrival (Slodzian *et al.*, 2004), electron multiplier aging, and extreme sensitivity to surface relief due to the short working distance (Fletcher *et al.*, 2008) are impediments to achieving the sub-permil accuracy and precision for natural abundance light-stable isotope analysis at micrometer-scale spatial resolution for which the large-radius multicollector CAMECA IMS 1280 SIMS (commonly called '1280', or simply, 'SIMS') instrument was designed (Valley & Kita, 2009). For example, a relation between instrumental bias and H/C was observed during $\delta^{13}C$ measurements of organic matter using a large-radius IMS 1270 (Sangély *et al.*, 2005, 2007), and the extent to which this affects NanoSIMS measurements is unknown or has yet to be reported. We refer the reader to Orphan & House (2009) for further detailed discussion of the relative merits of various SIMS techniques for geobiological investigations.

'Orientation effects', or measurable relations between instrumental bias and crystal orientation, can also adversely affect accuracy of SIMS measurements. In such cases, relatively high 'spot-to-spot' precision as measured on an individual standard grain in a single orientation may belie significant 'grain-to-grain' differences in bias that arise from different crystal orientations and thus degrade true accuracy. For example, orientation effects in sphalerite and galena lead to degraded precision and accuracy in $\delta^{34}S$ analyses of these minerals relative to analyses of pyrite made with the same instrumental settings, but for which there is no known orientation effect (Kozdon *et al.*, 2010). An orientation effect of several per mil has been observed in $\delta^{13}C$ measurements of individual graphite crystals in the WiscSIMS laboratory (T. Ushikubo, S. R. Dunn & J. W. Valley, unpubl. data). To our knowledge, the impact of orientation effects on NanoSIMS measurements of natural abundance stable isotope ratios remains unstudied. Here, we report our efforts using a large-radius IMS 1280 to develop a multiproxy approach for the detection of signs of life and planetary evolution in ancient geologic samples, an approach that in our view provides an optimal combination of spatial resolution, precision, and accuracy.

Geologic setting

The samples used in this study come from the Mount Bruce Supergroup, a 2.77–2.43 Ga package of sedimentary and volcanic rocks deposited in the Hamersley Basin on an Archean granite greenstone terrain within the Pilbara Craton of Western Australia (Trendall & Blockley, 1970; Blake *et al.*, 2004). Figs S1 and S2 in the Supplementary Information (SI) show a geologic map and composite stratigraphy, respectively.

These rocks are remarkably well preserved for their age, having been subjected only to prehnite-pumpellyite facies burial metamorphism at the basin scale and hydrothermal

alteration locally (Smith *et al.*, 1982; White *et al.*, 2014b). Samples were selected to document in greater detail the range of organic and isotope geochemical heterogeneity observed in several earlier studies of Neoarchean drill core from the Pilbara Craton, Western Australia (Ono *et al.*, 2003; Eigenbrode & Freeman, 2006; Kaufman *et al.*, 2007; Rasmussen *et al.*, 2008; Czaja *et al.*, 2010). Eleven samples ranging in age from ~2.5 to ~2.7 Ga were subsampled from the ABDP-9, WRL-1, RHDH2a, and SV-1 drill cores: Samples from the WRL-1, SV-1, and ABDP-9 drill cores are proximal to the depocenter of the Hamersley Basin, whereas samples from the RHDH2a core, drilled in the Ripon Hills area, likely represent the basin margin (Yamaguchi, 2002; Yamaguchi *et al.*, 2005; Eigenbrode & Freeman, 2006; Czaja *et al.*, 2010). Stratigraphic correlation and depositional age models are facilitated by impact spherule layers observed ~2.5 m below the Jeerinah/Marra Mamba contact near the depocenter in the main outcrop area (Hassler *et al.*, 2005) and ~60 m above the Jeerinah/Carawine contact near the margin in the Oakover River area (Rasmussen *et al.*, 2005). An important implication of this correlation is that the Carawine Dolomite in the Oakover River area represents carbonate deposition in a shelf setting that is time-equivalent to deeper water iron formation deposition in the Marra Mamba Fm located to the southwest (Eigenbrode, 2004; Eigenbrode & Freeman, 2006). On this basis, rocks from the RHDH2a and WRL-1 cores are considered to have been deposited along an increasing depth gradient across the basin. In that light, near-zero bulk δ^{56}Fe values near the center of the basin were previously interpreted to represent a dominance of hydrothermal and clastic Fe, whereas correlated low δ^{56}Fe and total Fe values on the margin suggest active dissimilatory iron reduction (Yamaguchi *et al.*, 2005; Czaja *et al.*, 2010).

SAMPLES AND METHODS

The following represents a summary of methods developed and applied during this study. The reader is encouraged to consult the detailed reporting of our methodology available in the supplementary material.

Descriptions of samples and standards

Samples

Sample selection for this study was guided by previously reported stratigraphic and bulk geochemistry data from the SV-1, RHDH2a, and WRL-1 cores (Eigenbrode & Freeman, 2006; Czaja *et al.*, 2010) and from the ABDP-9 core (Kaufman *et al.*, 2007), and we refer the reader to those publications for further contextual information about the specific sample depths discussed below. Locations of drill cores and their general stratigraphic contexts are shown in Figs S1 and S2.

Samples chosen for this study from the SV-1 core (55.3 and 126.4 m) come from the ~2.7 Ga Tumbiana Fm, a unit in the lower part of the Fortescue Group represented in deeper parts of the basin by shales (as is the case with these samples), and in shallower parts by (commonly stromatolitic) carbonates. One sample from the lower portion of the RHDH2a core (285.3 m) comes from the pyritic black shale of the Roy Hill Member of the ~2.6 Ga Jeerinah Fm, deposited in relatively deep water and located near the top of the Fortescue Group. A single sample from ~30 m higher in the RHDH2a core (252.2 m) represents shallower (shelf facies) deposition in the Carawine Dolomite (Eigenbrode & Freeman, 2006). Bulk inorganic carbon isotope values reported from this unit fall around $0 \pm 0.8‰$ (Shields & Veizer, 2002) and are interpreted to represent original Archean carbonate. Two samples of Wittenoom Formation (289.45 and 520.6 m), one sample from the Marra Mamba Formation (659.55 m) and one sample of the Jeerinah Fm (679.9 m), were taken from the WRL-1 core. Three samples of pyritic black shale in the Mount McRae Shale were taken from the ABDP-9 core: above (111.22 m), within (148.37 m), and below (161.02 m) the interval within which multiple geochemical proxies (including Δ^{33}S) were interpreted to record a transient episode, or 'whiff' of surface oxygenation (Anbar *et al.*, 2007; Kaufman *et al.*, 2007). Samples from the WRL-1, RHDH2a, and SV-1 cores were chosen to represent the wide range of published, bulk $\delta^{13}C_{org}$ values interpreted as evidence for Neoarchean aerobiosis (Eigenbrode, 2004; Eigenbrode & Freeman, 2006). Figure S1 shows the locations of drill cores sampled for this study, and Fig. S2 shows the relative position of the sampled units within composite Neoarchean stratigraphy of Western Australia. Reflected light and backscattered electron mosaic images of each sample with locations of individual SIMS targets are shown in SI (Figs S10–S18).

Existing SIMS standards

To optimize SIMS precision and accuracy, analyses of samples of unknown isotopic composition are bracketed by analyses of standard materials that, ideally, are mounted together with samples and meet the following criteria: (i) bulk isotopic composition is calibrated by 'conventional' analysis (e.g., by gas-source isotope ratio mass spectrometry), (ii) 'spot-to-spot' and 'grain-to-grain' isotopic composition is homogenous at the micrometer scale based on repeated SIMS analysis, and (iii) chemical composition and crystal structure (if applicable) is as similar as possible to the samples of interest (Valley & Kita, 2009). For sulfur isotope analyses in pyrite and carbon isotope analyses in calcite and dolomite, these criteria had been demonstrated in previous studies for working standards UWPy-1, Balmat pyrite with $\delta^{34}S = 16.04 \pm 0.18‰$ (all uncertainties are reported as ±2SD unless otherwise indicated),

$\Delta^{33}S = -0.003 \pm 0.009‰$, and $\Delta^{36}S = -0.21 \pm 0.24‰$ (Ushikubo *et al.*, 2014), UWC-3 calcite, which is from a granulite facies diopside-bearing calcite marble with $\delta^{13}C = -0.91 \pm 0.08‰$ (Kozdon *et al.*, 2009), and UW6220 dolomite with $\delta^{13}C = 0.79 \pm 0.71‰$ (Ferry *et al.*, 2010).

New standards for SIMS analysis of organic matter

For $\delta^{13}C$ analysis of organic matter by SIMS, establishing a suite of working standards was an important part of this study. Because systematic bias between H/C and $\delta^{13}C$ for SIMS analysis of organic matter had been previously observed in at least one other laboratory (Sangély *et al.*, 2005; Fig. S3, this study), a suite of materials representing the wide range of H/C variability in solid organic materials was assembled. To represent the low H/C end-member, a shungite (SH95S1a; Buseck *et al.*, 1997) and the oldest known coal, known as the Michigamme Anthracite (ca. 1840 Ma) UWMA-1 (Tyler *et al.*, 1957; Pufahl *et al.*, 2010) were chosen. Graphite was analyzed during our first session, but we do not recommend its use as a standard for organic carbon isotope analysis of amorphous organic materials including kerogen and pyrobitumen because it is a crystalline material, and we observe an orientation effect of several per mil. To represent the high H/C end-member, samples of Baltic and Dominican amber were used. Finally, a suite of coals was assembled from the research collection at Pennsylvania State University (PSU) to represent intermediate H/C values. These coals are identified as follows: DESC-21 (Lykens Valley #2 Seam, PA, USA), PSOC-1468 (Buck Mtn. Seam, PA, USA), PSOC-1534 (Waterfall Seam, AK, USA), UWLA-1 (LCNN Anthracite; Pappano, 2001), UWJA-1 (Jeddo Anthracite; Pappano, 2001), and UWHA-1 (Harmony Anthracite; Pappano, 2001).

Petrography and elemental analysis

Petrography was carried out on a Hitachi S-3400 variable pressure SEM in secondary electron (SE) mode to investigate morphology and backscattered electron (BSE) mode to investigate relative chemical heterogeneity based on grayscale of the BSE image (e.g. Figs S10–S18). Images were typically acquired with an accelerating voltage of 15 kV and a working distance of 5 mm (for best spatial resolution) or 10 mm (for EDS). Elemental composition of targets and associated minerals was measured in spot or mapping modes with an EDS detector (Thermo Scientific, Waltham, MA, USA) interfaced to the Hitachi S-3400.

Secondary-ion mass spectrometry

All SIMS measurements were performed using the CAMECA IMS 1280 large-radius multicollector ion microprobe in the WiscSIMS Lab., Department of Geoscience at the University of Wisconsin–Madison. Data in this study were gathered during eight separate analytical sessions. In general, we followed techniques described previously (Kita *et al.*, 2009; Valley & Kita, 2009; Williford *et al.*, 2011; Ushikubo *et al.*, 2014), and specific analytical conditions for the different applications discussed here are given in Table 2. In all cases, sample mounts were allowed to degas for 24–48 h in the 10^{-8} torr vacuum of the SIMS airlock (pressure in analytical chamber is 10^{-9} torr). A primary beam of $^{133}Cs^+$ was focused at the surface of the sample; beam diameter and intensity varied depending upon the technique, but total impact energy was always 20 keV (with a secondary-ion accelerating voltage of 10 keV). An electron gun oriented normal to the sample surface and gold coating provided charge compensation. Secondary ions of the major and minor isotope(s) were collected using Faraday cup detectors (with choice of resistor depending upon abundance, below), and relevant hydride ions were measured either simultaneously (e.g., $^{13}CH^-$) or by DSP2X scanning immediately after each analysis (e.g., $^{12}CH^-$, $^{32}SH^-$) with either electron multipliers (for low intensity beam conditions) or Faraday cup detectors (for high-intensity beam conditions). An electron multiplier was used to collect $^{13}C^-$ during small (1–3 μm) spot analyses. Each analysis consisted of intervals for (i) pre-sputtering (to penetrate gold coating and any minor surface contamination), (ii) centering secondary ions in the field aperture, and (iii) isotope ratio measurement.

Correction for 'bias', the sum of mass fractionation effects internal to the SIMS instrument, was achieved using an alpha correction as follows:

$$\alpha = (1000 + \delta^{13}C_{Raw})/(1000 + \delta^{13}C_{True}) \quad (1)$$

where α is bias, $\delta^{13}C_{Raw}$ is the uncorrected value for a standard analysis, and $\delta^{13}C_{True}$ is the value for the standard as determined by conventional, gas-source isotope ratio mass spectrometry (for sulfur isotope analysis, $\delta^{34}S$ is substituted for $\delta^{13}C$). Each set of ~10 unknown sample analyses was bracketed by eight analyses of a working standard (UWLA-1 for organic carbon, UWC-3 for calcite carbon, UW6220 for dolomite carbon, and UWPy-1 for pyrite sulfur). Bias and external precision are defined for each bracket as the average α, and two standard deviations (2SD, expressed in permil) of the eight standard analyses, respectively. Internal precision is defined as two standard errors (2SE) of the individual isotope ratios calculated from multiple measurement cycles within each analysis. Average count rate for the major ion (e.g. $^{12}C^-$ or $^{32}S^-$) was also calculated using the multiple measurement cycles in each analysis, and this ion count rate for each sample analysis is reported as a percentage relative to the average for the eight bracketing standard analyses as $^{12}C_{rel}$ or $^{32}S_{rel}$. Our experience with the analytical protocols and samples of this study suggests

that the intentional acquisition or interpretation of data at major ion count rates less than ~10% that of the standards should be avoided, as many possible confounding factors associated with SIMS analysis in mixed phases at low count rates can significantly degrade accuracy beyond the values reported here (see Table 1 and supplementary data).

For organic carbon analyses, bias correction was supplemented by an additional correction for H/C. To achieve this additional correction, multiple calibration standards with a wide range of H/C values (described above) were analyzed by gas-source isotope ratio mass spectrometry. Carbon isotopic and elemental compositions of standards, and bulk carbon isotope analysis methods are reported in the supplementary information. At the beginning of each SIMS organic carbon isotope analysis session, six to ten of these standards were analyzed multiple times, bracketed by analyses of the primary working standard UWLA-1. A linear regression was calculated using differential bias (α^*, or the ratio of the bias for a given organic standard to the bias for eight bracketing analyses of UWLA-1) and $^{13}CH^-/^{13}C^-$ (a proxy for H/C, measured simultaneously during each individual SIMS $\delta^{13}C$ analysis) as the dependent and independent variables, respectively. Differential bias is defined as the ratio of bias for each calibration standard to bias for UWLA-1 during the calibration routine, and this method permits calculation of α^* for each sample analysis using $^{13}CH^-/^{13}C^-$. For each $\delta^{13}C$ analysis of sample organic matter, total bias correction (including H/C correction), was achieved using the following equation:

$$\delta^{13}C = (1000 + \delta^{13}C_{Raw})/(\alpha \times \alpha*) - 1000. \quad (2)$$

Relative bias regression data and 95% confidence interval uncertainty calculations are reported in supplementary data. A quadratic propagation of uncertainty including external precision of bracketing standards, internal precision of individual analyses (affected in some cases by natural inhomogeneity at the scale of an individual analytical pit), and relative bias correction is also reported in supplementary data tables, as u_c. For sulfur isotope analysis and carbon isotope analysis of carbonates, bias correction was achieved as above, but without inclusion of the α^* term (and substitution of $\delta^{34}S$ for $\delta^{13}C$).

RESULTS AND DISCUSSION

Data for SIMS $\delta^{13}C$ analyses of organic matter, calcite, and dolomite, as well as $\delta^{34}S$ and $\Delta^{33}S$ of pyrite are plotted against estimated age in Fig. 1 ($\Delta^{36}S$ data, acquired from only five of ten samples, are omitted). To maximize the clarity of this large and complex data set, we have combined the presentation of results with our interpretations. A key consideration from the outset of this study has been to present our data in a way that maximizes their relevance as the interpretive context inevitably evolves and facilitates target relocation for future analysis. To that end, we report every SIMS analysis in order of acquisition, for samples and standards in a supplementary data file. Reflected light and backscattered electron images of each SIMS sample mount are reported in a separate supplementary file, with all targets in each sample labeled (Figs S10–S18). Higher magnification SEM images of each analyzed target (acquired after analysis whenever possible to show analytical pits) are also provided in this supplementary file (Fig. S19). These post-analysis images allow the isotopic data reported here to be interpreted in the context of analyte morphology and associated mineralogy. The supplementary data file also includes additional bulk geochemical data for standards and samples, as well as bias vs. H/C calibration data and uncertainty analysis.

Organic carbon isotope analysis

New organic carbon isotope standards for SIMS

In session 1, beginning on December 14, 2010, ten organic materials whose bulk $\delta^{13}C$ had been measured

Table 1 Information about five carbon isotope and three sulfur isotope analysis sessions at the WiscSIMS secondary-ion mass spectrometry facility that generated data for this study. Average external precision (at two standard deviations) for each session is indicated as $2SD_{std}$

Start date	No.	Purpose	Spot size (μm)	Standard	$2SD_{std}$ (‰)
12/14/2010	1	$\delta^{13}C$ organic matter	6 μm	UWLA-1	0.34
4/19/2011	2	$\delta^{13}C$ organic matter	6 μm	UWLA-1	0.36
6/14/2011	3	$\delta^{13}C$ organic matter	6 μm	UWLA-1	0.38
7/19/2011	4	$\delta^{13}C$ organic matter	3 μm	UWLA-1	0.82
1/25/2012	5	$\delta^{34}S$ pyrite	10 μm	UWPy-1	0.30
1/25/2012	5	$\Delta^{33}S$ pyrite	10 μm	UWPy-1	0.12
6/19/2012	6	$\delta^{34}S$ pyrite	10 μm	UWPy-1	0.35
6/19/2012	6	$\Delta^{33}S$ pyrite	10 μm	UWPy-1	0.09
7/17/2012	7	$\delta^{13}C$ calcite	8 μm	UWC-3	0.87
7/17/2012	7	$\delta^{13}C$ dolomite	8 μm	UW6220	0.65
8/15/2012	8	$\delta^{34}S$ pyrite	20 μm	UWPy-1	0.26
8/15/2012	8	$\Delta^{33}S$ pyrite	20 μm	UWPy-1	0.05
8/15/2012	8	$\Delta^{36}S$ pyrite	20 μm	UWPy-1	0.79

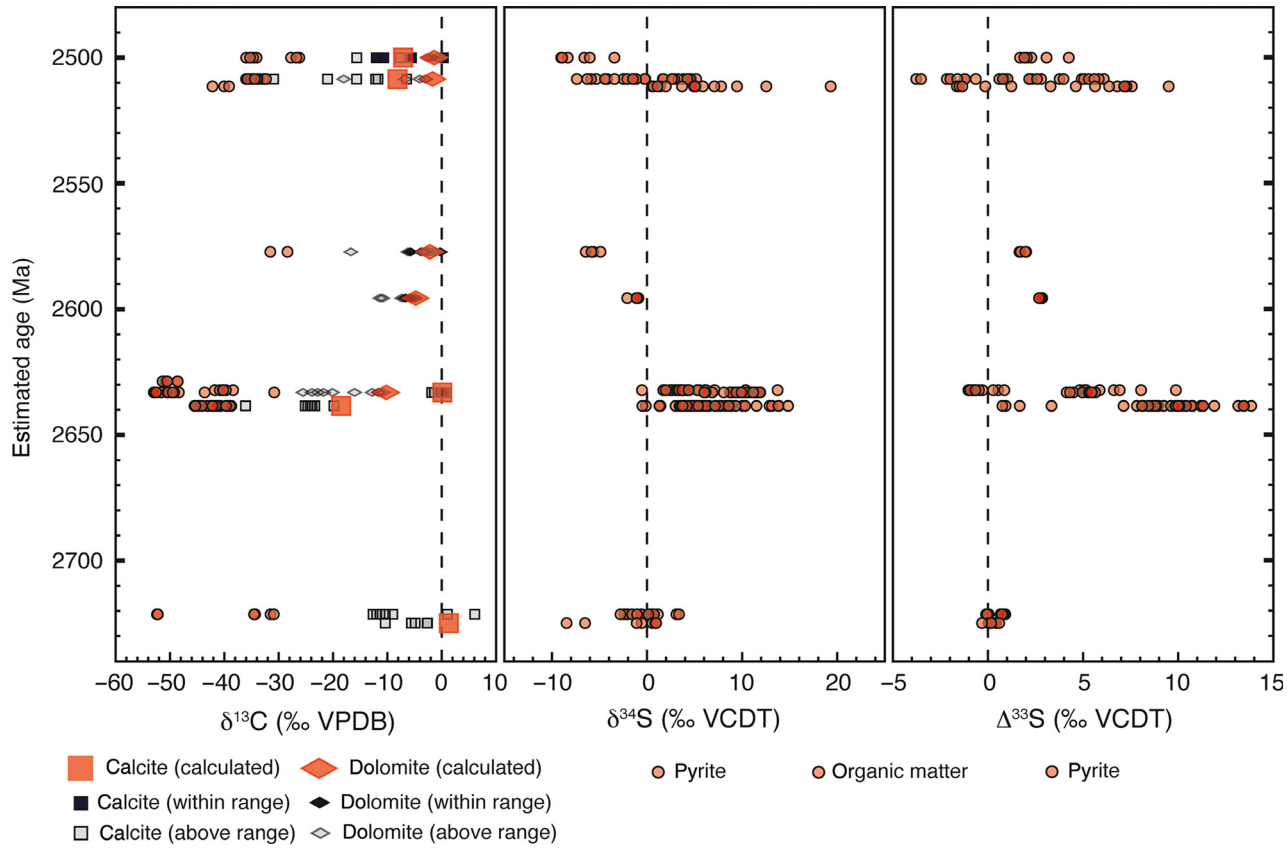

Fig. 1 Data from SIMS *in situ* carbon isotope analysis of organic matter, dolomite, and calcite, and SIMS sulfur three-isotope analysis of pyrite in ten Neoarchean samples ranging in age from ~2.7 to ~2.5 Ga. Samples were previously analyzed for bulk carbon and iron isotopes by Eigenbrode & Freeman (2006) and Czaja *et al.* (2010), respectively, and estimated age is assigned based on the model by Czaja *et al.* (2010). SIMS carbon isotope analyses of calcite and dolomite that had ^{12}C count rates higher than the average for organic-free standards likely sampled organic inclusions and are labeled 'above range' (small, gray squares and diamonds). Analyses with count rates at or slightly below standard values likely sampled organic-free domains and are labeled 'within range' (small, black squares and diamonds). Linear correlations between ^{12}C count rate and $\delta^{13}C$ were used to calculate $\delta^{13}C$ of calcite (large squares) and dolomite (large diamonds) for individual samples (see text).

previously by elemental analyzer continuous flow isotope ratio mass spectrometry (EA-CF-irMS) were analyzed by WiscSIMS to identify the material with the greatest spot-to-spot and grain-to-grain micrometer-scale carbon isotopic homogeneity. This was employed as a primary working standard for organic carbon isotope analysis with two FC detectors, and to determine whether H/C and bias are correlated on the WiscSIMS instrument as had been previously observed in another laboratory (Sangély *et al.*, 2005). That study used Fourier transform infrared spectroscopy to analyze the aliphaticity (as a proxy for H/C) of each organic target after SIMS analysis. The alternative technique we report here has the significant advantage that H/C proxy data are acquired simultaneously with $^{13}C/^{12}C$ ratios. Multiple grains of each of the organic carbon standards were analyzed in this session, with the exception of the two ambers, added later as high H/C end-members.

Graphite UWGr-1 was prepared as a powder from a graphite rod used for carbon arc coating with the intention to randomize crystal orientations and thus minimize orientation effects. Small 'clumps' of graphite powder that had been epoxy-mounted together with potential standards were analyzed three to four times each, and these showed high apparent heterogeneity (4‰; 2SD). We have considered whether the unexpectedly high heterogeneity we observed in graphite powder was due to variable inclusion of epoxy (that would have penetrated along grain boundaries during sample preparation) during individual analyses. Three analyses of UWGr-1 have $\delta^{13}C_{Raw}$ from −58 to −59.5‰, and the other seven analyses have $\delta^{13}C_{Raw}$ between −62 and −63‰, similar to epoxy in this standard mount that has $\delta^{13}C_{Raw} = -63.6 \pm 0.4$‰ ($n = 4$). However, values of $^{13}CH/^{13}C$ for UWGr-1 range from 0.008 to 0.017, whereas values for epoxy are much higher and range from 0.138 to 0.140. We observe no correlations between $^{13}CH/^{13}C$ or ^{12}C count rate and $\delta^{13}C_{Raw}$ for UWGr-1: We thus attribute the three anomalous analyses to true heterogeneity in the graphite.

Table 2 Micrometer-scale heterogeneity of nine organic materials analyzed during the first organic carbon isotope analysis session at WiscSIMS. UWLA-1 was chosen as the primary working standard. Bulk $\delta^{13}C$ values for each material are listed in the supplementary data file

Material	Grains	Spots	2SD (‰)
UWLA-1	3	18	0.34
UWMA-1	3	18	0.35
UWJA-1	3	18	0.38
UWRA-1	3	18	0.46
Epoxy	n/a	6	0.60
UWHA-1	3	18	0.91
PSOC-1468	3	18	1.00
DESC-21	3	9	1.14
PSOC-1534	3	10	1.46

Because of this heterogeneity and an orientation effect observed previously, we rejected graphite as a standard for SIMS $\delta^{13}C$ analysis of amorphous organic matter in this study.

The number of grains analyzed, total number of spots, and 2SD heterogeneity for each material observed during this session are shown in Table 2. UWLA-1, prepared from LCNN anthracite, was chosen as the primary working standard due to its high spot-to-spot and grain-to-grain homogeneity (average 0.34‰ 2SD). This material enables external precision with SIMS organic carbon isotope analysis with a 6-μm spot that is comparable to bulk carbon isotope analysis with EA-CF-irMS. To further constrain the bulk $\delta^{13}C$ of this material, three individual grains of UWLA-1 were analyzed separately at Wisconsin using the sealed quartz tube method and a dual-inlet gas-source mass spectrometer (Kitchen & Valley, 1995). The results of these three analyses were remarkably consistent at −23.56‰, varying by <0.01‰. Typical precision for this method with multiple analyses of USGS24 graphite is ±0.15‰ (2SD); thus, we report the bulk $\delta^{13}C$ of UWLA-1 to be −23.56 ± 0.15‰ (2SD).

During the second session, beginning April 19, 2011, seven of the ten potential standards analyzed during the first session were reanalyzed, and the two ambers were analyzed for the first time. Eighteen analyses on three grains of Baltic amber had a 2SD heterogeneity of 0.68‰, and eighteen analyses on three grains of Dominican amber had a 2SD heterogeneity of 1.2‰. Analyses of $\delta^{13}C$ and $^{13}CH/^{13}C$ were used to generate the first $^{13}CH/^{13}C$ vs. bias working curve during this session. We observed a strong correlation, as shown in Fig. S3. This correlation demonstrates an effect of H/C on bias of up to 4‰ (expressed in per mil as $(\alpha - 1)$ *1000), indicating that monitoring this effect is particularly important when sub-permil accuracy is required. The validity of this approach is supported by correlation between $^{13}CH/^{13}C$ and H/C of the six standard materials for which we have bulk H and C abundance data. As is the case with any SIMS method, accuracy is optimized using frequent measurements of a running standard and calibration against standards that are as chemically similar to the sample as possible. The novel H/C correction method reported here, incorporating simultaneous collection of $^{12}C^-$, $^{13}C^-$, and $^{13}CH^-$, allows the efficient use of a single 'running' standard after an initial calibration sequence.

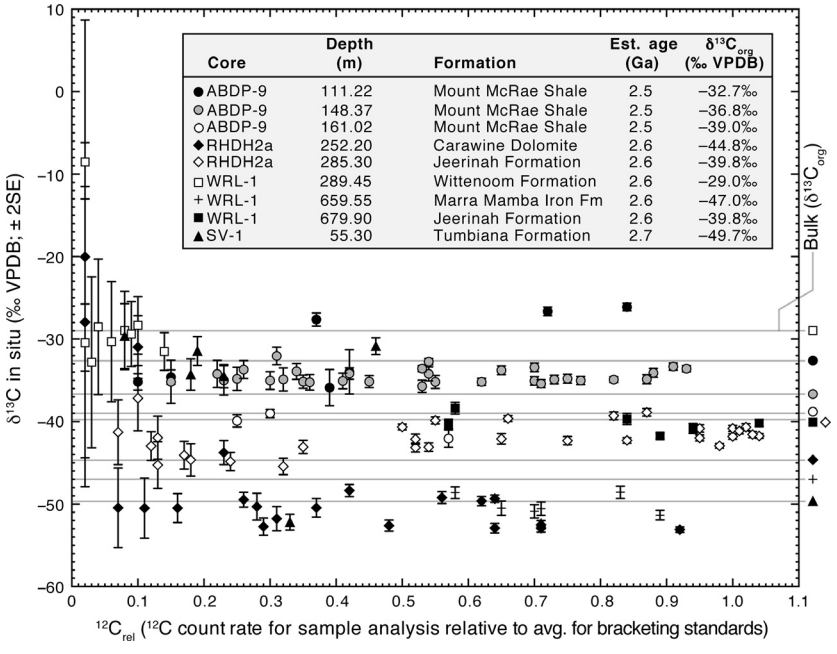

Fig. 2 SIMS $\delta^{13}C$ data for all analyses reported here, plotted against ^{12}C count rate relative to average for UWLA-1 (anthracite) bracketing standard. Error bars show internal precision (± two standard error; 2SE) that decreases as expected with decreasing ^{12}C count rate. Horizontal gray lines indicate bulk $\delta^{13}C$ values for each sample.

Systematic offsets and ion count rates

Data from all analytical sessions for $\delta^{13}C$ of Neoarchean organic matter are shown in Fig. 2. The $\delta^{13}C$ data in Fig. 2 are plotted against $^{12}C_{rel}$, or the $^{12}C^-$ count rate of an individual analysis relative to the average count rate of the eight corresponding bracketing standard analyses (of UWLA-1). For the data set as a whole, we do not observe any systematic offset between bulk $\delta^{13}C$ and our SIMS measurements in this study. For example, SIMS $\delta^{13}C$ data for ABDP-9 148.37 are higher, and for RHDH2a 285.30 are lower than the respective bulk values for these samples. Nor do we observe a systematic change in SIMS $\delta^{13}C$ with decreasing $^{12}C^-$ count rate. For $^{12}C^-$ count rates between 15% and 93% of bracketing standards, data for ABDP-9 148.37 range within ~2‰ of the average for the sample. Internal precision, or two standard errors (2SE) of the 20 measurement cycles comprising an analysis, is also shown for each analysis in Fig. 2. Internal precision is controlled by counting statistics and signal-to-noise ratio as well as any natural isotopic heterogeneity encountered with depth in a single analysis pit. The decrease in internal precision with $^{12}C_{rel}$ is apparent in Fig. 2. Although precision is poor at low count rates, acceptable accuracy may be possible to achieve in aggregate. Nine analyses in a sample of the Wittenoom Formation (WRL-1 289.45) have $^{12}C_{rel}$ count rates lower than 15%, with an average of 6%. When the analysis with the lowest count rate (2%; *n.b.* $\delta^{13}C_{Raw}$ for this analysis is 20‰ higher than any of the others in

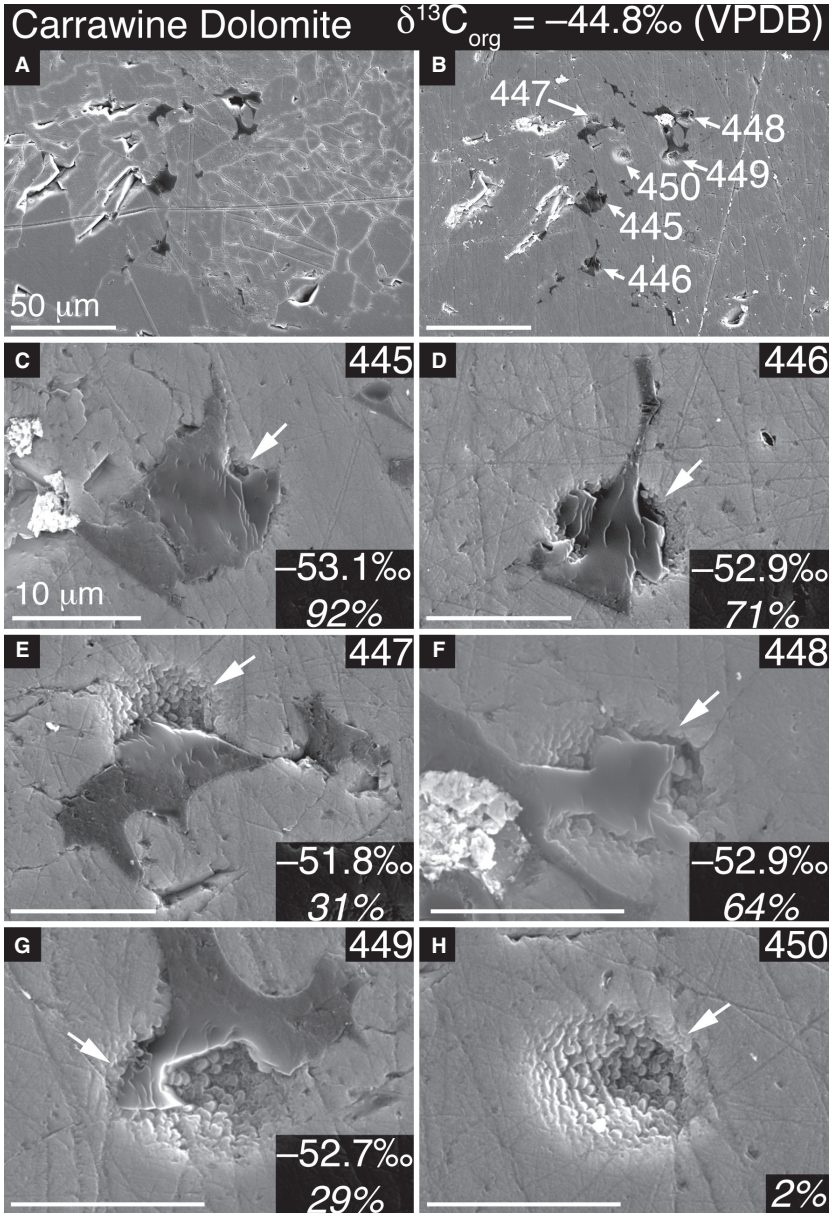

Fig. 3 Secondary electron images showing a ~0.03-mm^2 region of the Carawine Dolomite (RHDH2a 252.2 m) before (A) and after (B) SIMS $\delta^{13}C$ analysis. Enlargements (B–H) show analytical pits (pit edges indicated with white arrows) from five analyses of varying proportions of pyrobitumen and calcite matrix and one analysis of apparently organic-free calcite (H). Individual analysis numbers are indicated at the top right, and $\delta^{13}C$ (‰ VPDB) and ion count rate relative to UWLA-1 (anthracite) standard ($^{12}C_{rel}$) are indicated at bottom right of each panel. Due in part to low ionization efficiency of inorganic relative to organic carbon, pure calcite yields only 2% of the ^{12}C counts yielded by pure organic matter, and values of $\delta^{13}C$ for these analyses are within uncertainty at organic:inorganic carbon ratios as low as 30%. Scale bars are 50 μm in (A) and (B), and 10 μm in (C–H).

the sample) is rejected, the remaining eight analyses have $\delta^{13}C = -30.0 \pm 4.5‰$, only 1‰ different (lower) than the bulk value for this sample.

SIMS $\delta^{13}C$ analysis of organic matter in carbonate matrices

Kerogen in a sample of the Carawine Dolomite (RHDH2a 252.2, Fig. S14) occurs in stylolites associated with dolomite and pyrite (Fig. S7, SI). Pyrobitumen in this sample (Figs 3, S7, S14) is concentrated along cracks in a prominent calcite vein, and is sometimes associated with quartz. This pyrobitumen has $\delta^{13}C$ that is ~3‰ lower ($-52.6 \pm 0.8‰$; targets 4 and 5, Figs S14, S19), as well as a lower H/C ($^{13}CH/^{13}C = 0.65$) than the average for kerogen in this sample ($-49.8 \pm 1.4‰$; $^{13}CH/^{13}C = 0.78$; targets 6–10, Figs S14, S19). By contrast with pyrobitumen in the Mt. McRae Shale samples (ABDP-9; discussed below), the difference in both $\delta^{13}C$ and H/C, as well as the modes of occurrence of pyrobitumen and kerogen in the Carawine Dolomite sample, is consistent with post-depositional introduction of pyrobitumen together with vein-fill calcite, whereas the kerogen now concentrated in stylolites is more likely to be syndepositional. Rasmussen (2005) interpreted pyrobitumen nodules and streaks as evidence for petroleum generation and migration in the Jeerinah Fm and suggested that the pyrobitumen was locally sourced as a result of burial maturation <2.45 Ga. Peak metamorphism and metasomatic alteration of the Mount Bruce Supergroup coincided with a generally northward migration of hydrothermal fluids as a result of the collision of the Pilbara and Yilgarn cratons during the Capricorn orogeny <2.2 Ga (Rasmussen *et al.*, 2005; White *et al.*, 2014a). It is possible that (pyro)bitumen was redistributed or emplaced in the Carawine Dolomite as a result of this event. A similar inference of large-scale migration has been made for vein pyrobitumen with higher $\delta^{13}C$ than the *in situ* kerogen in the Jeerinah Fm on the basis of NanoSIMS analyses (Rasmussen *et al.*, 2008).

Five analyses of varying amounts of pyrobitumen in a calcite matrix made during session 2 indicate that Wisc-SIMS organic carbon isotope analysis of organic domains in carbonate using the 6 μm, two FC techniques at count rates as low as 30% (i.e., 30% organic matter in carbonate) of the average for the working standard are possible with near permil accuracy (Fig. 3). Four of these five analyses of pyrobitumen in calcite (with $^{12}C_{rel}$ from 0.92 to 0.29) are tightly distributed along a linear trend of $\delta^{13}C$ vs. $^{12}C_{rel}$ indicating a positive shift of only 0.4‰ from the highest to lowest count rate. A single analysis with $^{12}C_{rel} = 0.31$ indicates a positive shift of 1.3‰ from the analysis with the highest count rate.

One analysis of an organic carbon-free domain of calcite adjacent to pyrobitumen has a count rate only 2% that of the working standard carbonate carbon relative to organic carbon with this SIMS technique. Multiple factors are likely responsible for the low relative C^- production in carbonate relative to organic carbon. Calcite and dolomite are ~12 and 13% C by mass, compared to typical sedimentary organic matter that is 60 to >90% C by mass. Carbonate carbon also has a lower ionization efficiency than organic carbon (see further discussion below). A mixing model (not shown) assuming a ~40‰ difference in inorganic and organic $\delta^{13}C$ and a 2% contribution from calcite suggests that the threshold for sub-permil accuracy would be $^{12}C_{rel} = 0.5$. Work continues to understand the constraints to accuracy in SIMS $\delta^{13}C$ analysis of small organic domains in carbonate, and the possible applications are numerous.

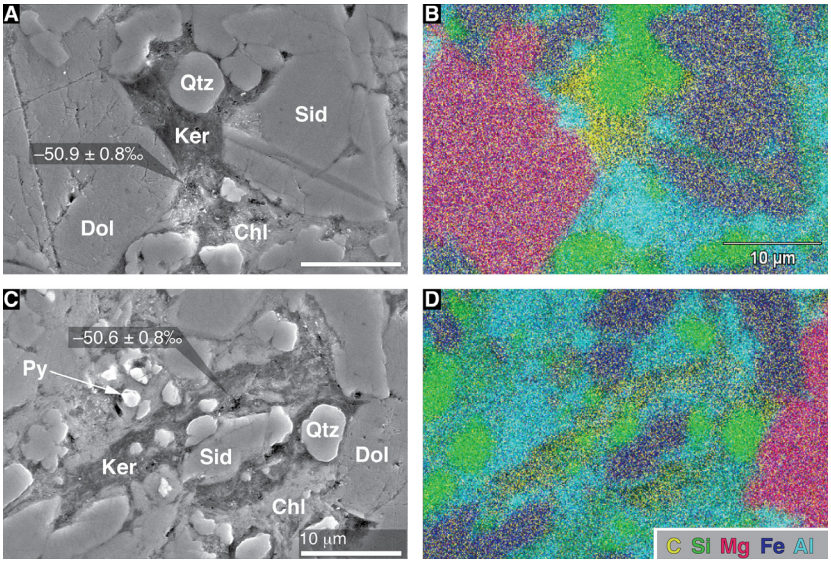

Fig. 4 Secondary electron images (A, C) and energy-dispersive x-ray spectroscopic elemental maps (B, D) small (3 μm) spot $\delta^{13}C$ analyses (‰ VPDB ± 2SD external precision) of typical kerogen (ker) in a shale sample from the ~2.6 Ga Marra Mamba Iron Formation (WRL-1 659.55 m). Kerogen in this sample is associated with dolomite (Dol), siderite (Sid), quartz (Qtz), chlorite (Clc), pyrite (Py). Pressure solution features and micrometer-scale veining are apparent at intersections between quartz and siderite in (A). Scale bars are 10 μm.

Spatial resolution and heterogeneity

A total of 121 organic targets in nine Neoarchean samples ranging in age from ~2.7 Ga to ~2.5 Ga were analyzed in this study. Most targets were analyzed using a 6-μm-diameter beam and Faraday cup detectors for both $^{12}C^-$ and $^{13}C^-$. To investigate the limits of spatial resolution for the instrument, we analyzed six targets each in samples of the Marra Mamba Iron Fm (WRL-1 659.55 m) and the Jeerinah Fm (WRL-1 679.90 m) with a 3-μm-diameter beam, using an electron multiplier for $^{13}C^-$ (Fig. 4). Average SIMS $\delta^{13}C$ values in these two samples are 3.1 and 0.4‰ lower than bulk $\delta^{13}C$ values, respectively, and we have no reason to suspect a decrease in accuracy with the smaller beam condition (although external precision using this condition is not as good as the larger, 6 μm diameter condition due to fewer secondary ion counts). We started this session using a 1-μm-diameter beam to analyze 1 μm or smaller targets; however, the ~1 μm uncertainty in stage motion (due to backlash) combined with our inability to resolve 1-μm features in the optical system of the IMS 1280 made targeting difficult. To compensate for this difficulty, we increased the size of the beam to 3 μm, which can be imaged during analysis, and generated $^{13}C^-$ ion images (Fig. S6) prior to analysis to facilitate accurate aiming. Software (digital zoom) and hardware (optical registering at 0.1-μm scale), and optical (365-nm sample illumination, Kita *et al.*, 2015) improvements in the WiscSIMS instrument made after completion of this study have improved targeting, and we frequently achieved 1 μm targeting accuracy in later efforts, although analysis spots should always be verified by SEM. Figure 4 shows representative targets and analytical pits for small spot $\delta^{13}C$ analysis in sample WRL-1 659.55 m.

The analytical techniques presented here are designed to evaluate micrometer-scale variability, including correlations between isotopic composition and morphology, mineralogy, and elemental compositions, and in this study we report several such correlations that are invisible to bulk techniques. However, given (i) a sufficient number of SIMS analyses, (ii) sufficient accuracy of SIMS analyses, and (iii) sufficient sampling of characteristic phases in a particular sample, then the average SIMS value should be similar to the bulk value for that sample. In this study, bulk $\delta^{13}C$ values and averaged SIMS $\delta^{13}C$ values are remarkably consistent. The difference between the averaged SIMS value and the bulk value was calculated for each sample, and the average of these calculated differences is 0.02‰.

It is important to distinguish apparently random heterogeneity observed in SIMS data (that could simply indicate poor precision and/or accuracy) from systematic variability that can be correlated to textures or compositions (and is a signature of a natural process operating in the sedimentary or diagenetic system). Five of the nine samples analyzed in this study had a range in SIMS $\delta^{13}C$ of less than 5‰, and the average range is 7.4‰ (Table 3). A sample of the ~2.7 Ga Tumbiana Fm exhibits the most dispersion observed in this study, and the dispersion is demonstrably real by systematic correlation to textures. A single kerogenous domain associated with filamentous TiO_2 has $\delta^{13}C = -52.3 \pm 0.1$‰ ($n = 2$), consistent with the lowest values reported in earlier studies of Tumbiana Fm drill core (Eigenbrode & Freeman, 2006; Thomazo *et al.*, 2009a), suggesting a metabolically recycled, methanotrophic carbon source. More typical kerogen observed in this sample, associated with clay minerals and pyrite, has $\delta^{13}C = -32.8 \pm 3.6$‰ ($n = 4$; e.g., Fig. 5). This kerogen component is isotopically similar to a relatively high $\delta^{13}C$ organic component in the Tumbiana Fm identified by earlier bulk measurements (Eigenbrode & Freeman, 2006; Thomazo *et al.*, 2009a), and likely derives from the bio-

Table 3 Average and range of SIMS $\delta^{13}C$ measurements of organic matter and/or carbonate minerals in eleven Neoarchean rock samples. Values of $\delta^{13}C$ for dolomite ($\delta^{13}C_{dol}$ calc) and calcite ($\delta^{13}C_{cal}$ calc) were estimated for samples that contained varying degrees of inter- and intracrystalline organic matter in analyzed carbonate domains that likely drives linear relations between $\delta^{13}C$ and ^{12}C count rate relative to organic-free bracketing standards by assuming carbonate $\delta^{13}C$ homogeneity and using an interpolated value at $^{12}C_{rel} = 1.0$. These values were then used to calculate the average offset between organic carbon, calcite ($\Delta^{13}C_{cal\text{-}org}$) and/or dolomite ($\Delta^{13}C_{dol\text{-}org}$) for each sample

Core	Depth (m)	Unit	Est. Age (Ma)	$\delta^{13}C_{org}$ (‰ VPDB) Max	Min	Avg	n	$\delta^{13}C_{dol}$ calc (‰)	$\Delta^{13}C_{dol\text{-}org}$ (‰)	$\delta^{13}C_{cal}$ calc (‰)	$\Delta^{13}C_{cal\text{-}org}$ (‰)
ABDP-9	111.22	Mount McRae	2500	−26.2	−36.0	−31.5	7	−1.4	30.1	−7.1	24.4
ABDP-9	148.37	Mount McRae	2500	−32.3	−36.0	−34.8	32	−1.7	33.2	−11.2	23.6
ABDP-9	161.02	Mount McRae	2500	−39.1	−42.2	−40.4	3	n.d.	n.d.	n.d.	n.d.
WRL1	289.45	Wittenoom	2577	−28.4	−31.5	−30.0	2	−2.2	27.8	n.d.	n.d.
WRL1	520.6	Wittenoom	2596	n.d.	n.d.	n.d.	n.d.	−2.2	n.d.	n.d.	n.d.
WRL1	659.55	Marra Mamba	2629	−48.6	−51.4	−50.1	6	n.d.	n.d.	n.d.	n.d.
WRL1	679.9	Jeerinah	2632	−38.4	−41.7	−40.2	6	n.d.	n.d.	n.d.	n.d.
RHDH2a	252.2	Carawine	2633	−30.8	−53.0	−49.5	19	−9.0	40.5	0.5	50.0
RHDH2a	285.3	Jeerinah	2639	−38.7	−45.5	−42.1	28	n.d.	n.d.	−18.5	23.6
SV1	55.3	Tumbiana	2721	−30.9	−52.4	−39.3	6	n.d.	n.d.	−10.9	28.4
SV1	126.4	Tumbiana	2725	n.d.	n.d.	n.d.	n.d.	n.d.	n.d.	−9.0	n.d.

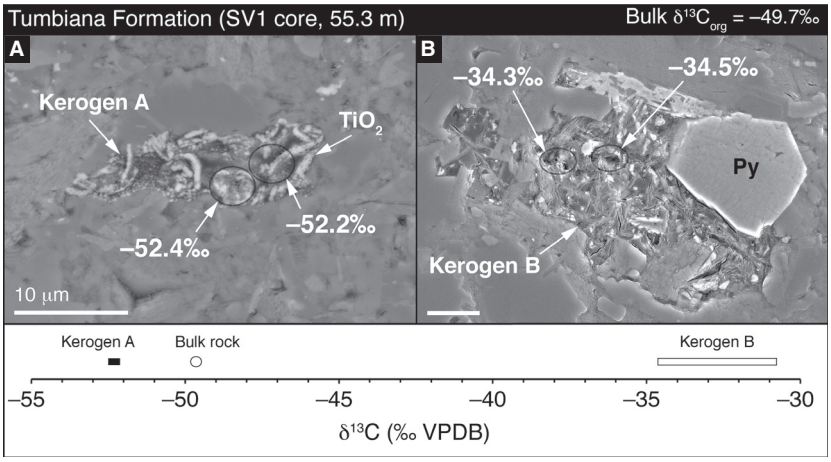

Fig. 5 Two types of kerogen situated ~6 mm apart in a single sample of pyritic shale from the ~2.7 Ga Tumbiana Formation (SV-1 55.3 m; Fig. S16) indicating the preservation of multiple metabolic signatures. Type A kerogen is associated with filamentous TiO_2 and has low $\delta^{13}C$. Type B kerogen is associated with clay minerals and pyrite (Py), and has higher $\delta^{13}C$. Values of $\delta^{13}C$ for these two different kerogen types bound the bulk rock value for this sample as shown at the bottom. Scale bars are 10 μm.

mass of primary producers. These two classes of organic matter show no evidence of post-depositional migration into the sample and are likely to have been end-members of a complex microbial ecosystem: photosynthetic primary producers inhabiting surface waters (high $\delta^{13}C$) and methanotrophs inhabiting sediments (low $\delta^{13}C$). These

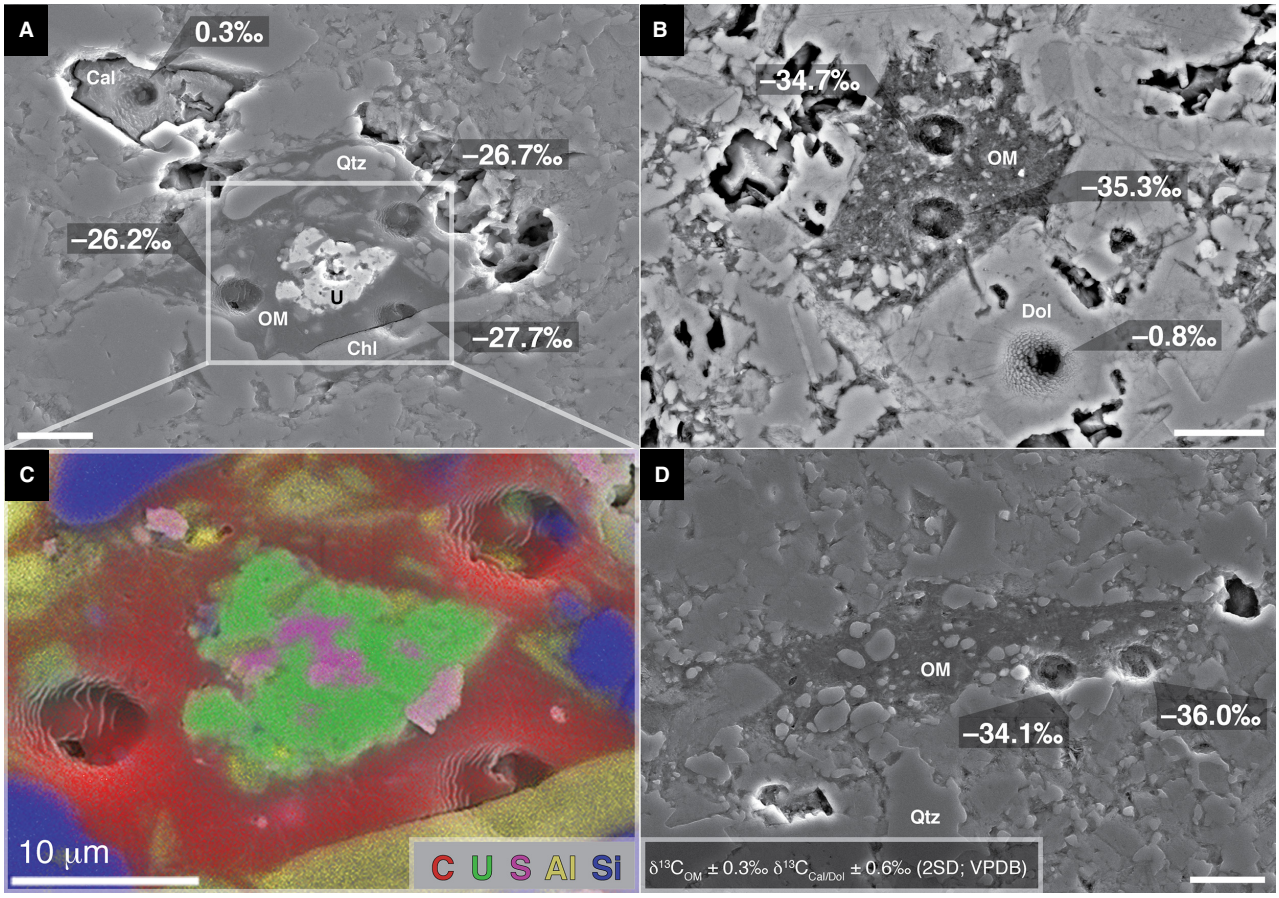

Fig. 6 Secondary electron (A, D), backscattered electron (B), and energy-dispersive x-ray spectroscopic elemental map (C) of pyrobitumen (OM) surrounding a uraniferous (U) mineral grain (A, C) and typical kerogen (B, D) in a sample of the Mount McRae Shale (ABDP-9 111.22 m). Analytical pits from SIMS $\delta^{13}C$ analysis of organic matter (OM), calcite (Cal) and dolomite (Dol) are shown, and external precision for these analyses is indicated at lower right in panel (D). Pyrobitumen in this sample is associated with detrital quartz (Qtz) and chlorite (Chl), and is ~8‰ higher in $\delta^{13}C$ than co-occurring kerogen in this sample, the latter suggesting either a different source or alteration mechanism for these two organic components in the sample. Calcite in this sample is likely secondary, but the offset between dolomite and kerogen $\Delta^{13}C_{Dol-ker}$ provides an estimate of the apparent metabolic fractionation: ~34‰. Scale bars are 10 μm.

two classes of organic matter in close spatial association that are (i) indigenous and syngenetic, and (ii) distinct in morphology, associated mineralogy, and carbon isotopic composition represent a robust biosignature (Lepot *et al.*, 2013; Williford *et al.*, 2013).

The bulk $\delta^{13}C$ value for this sample of the Tumbiana Fm is −49.7‰, suggesting that the low-$\delta^{13}C$ phase we observed, or another similar phase is relatively abundant but may typically occur in nanometer-scale domains that we did not sample (and would be too diffuse for accurate SIMS analysis). This highlights an important difference between spatially resolved SIMS analysis and bulk analysis: although the former potentially yields far higher 'information density' by increasing spatial resolution, a selection bias introduced by analysis parameters (SIMS beam diameter, spatial resolution of light, and electron microscopy techniques, etc.) may cause important phases to be overlooked. Complementary molecular analyses, such as H/C and N/C mapping with NanoSIMS (Wacey *et al.*, 2010), micro-Raman, or X-ray absorption spectroscopy (Lepot *et al.*, 2009), may help to track distinct micro-reservoirs of organic matter and constrain their importance in the studied rocks. Bulk and spatially resolved analyses are complementary, and an integrated approach will maximize the information yield for a sample.

Sample ABDP-9 148.37b contains pyrobitumen nodules surrounding central sulfide grains, and these domains have slightly higher $\delta^{13}C$ (−33.2 ± 0.4‰) than, but similar H/C ($^{13}CH/^{13}C$ = 0.069) to the average for kerogen in this sample (−35.0 ± 0.8‰; $^{13}CH/^{13}C$ = 0.066). A similar pyrobitumen nodule with a central uranium-rich grain (Fig. 6A,C) in ABDP-9 111.22 was analyzed three times, and it has significantly higher $\delta^{13}C$ (−26.9 ± 0.8‰) than the average for kerogen in the sample (−35.0 ± 0.8‰), but H/C ($^{13}CH/^{13}C$) in pyrobitumen is also similar (0.068) to kerogen (0.066). This 8‰ enrichment in ^{13}C observed in the Mount McRae pyrobitumen is larger than can be explained by typical thermal maturation processes (Des Marais, 2001). Similar associations in the Jeerinah Fm have been previously reported as evidence for Archean petroleum generation (Rasmussen, 2005), and it is possible that the ^{13}C enrichment observed here resulted from radiolytic alteration of pyrobitumen, as has been proposed for the uraniferous Cigar Lake (Landais *et al.*, 1993) and Athabasca (Sangély *et al.*, 2007) deposits. Alternatively, the U-associated pyrobitumen observed in ABDP-9 111.22 may originate from another source rock.

Pyrobitumen nodules such as those described above do not occur in the oldest sample of the Mount McRae shale analyzed in this study (ABDP-9 161.02). Organic matter in this sample occurs in cores of 'nodular' associations of siderite and pyrite (Fig. 7C–D) and has low $\delta^{13}C$ (−40.4 ± 1.6‰). A single large pyrobitumen nodule surrounding a small (~3 μm) central grain of chalcopyrite, and associated with chlorite and pyrite, was observed in a sample of the Jeerinah Formation (RHDH2a 285.3#1;

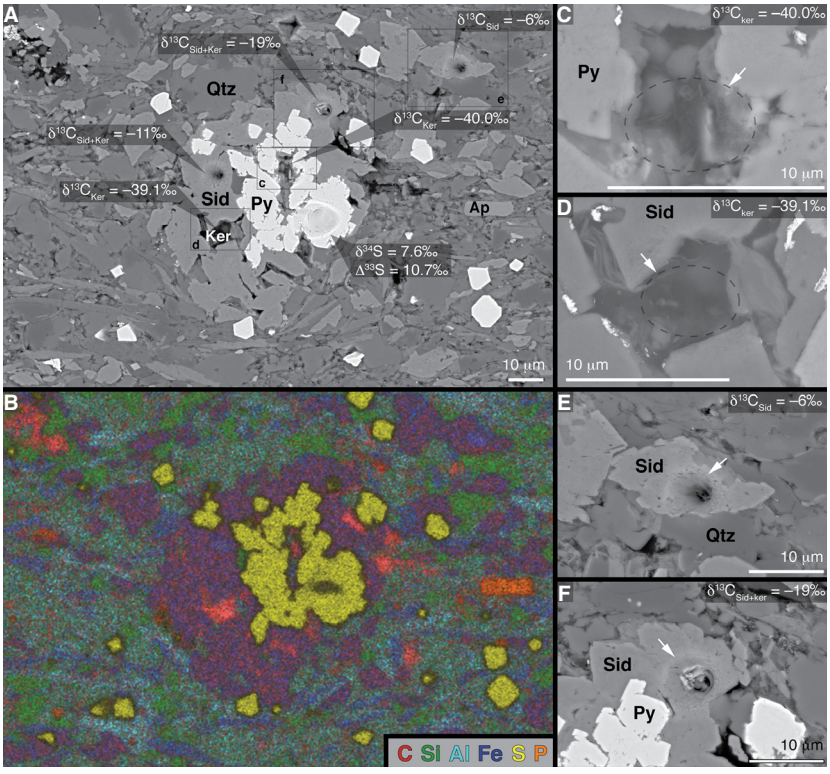

Fig. 7 (A, C–F) Backscattered electron images of nodula association of siderite (Sid), pyrite (Py), and kerogen (Ker) surrounded by detrital quartz (Qtz) and clay minerals in a sample of the ~2.5 Ga Mount McRae Shale (ABDP-9 161.02 m). Analytical pits and data from sulfur three-isotope analysis of pyrite (‰ VCDT), and carbon isotope analyses of kerogen and siderite (‰ VPDB) are indicated. Energy-dispersive spectroscopy elemental map is shown in (B). Enlargements of kerogen (C, D) and siderite (E, F) domains are shown at right. Analysis shown in (E) is sampled only siderite, but analytical pit shown in (F) penetrated siderite grain and intersected kerogen, yielding a higher ^{12}C count rate and lower, mixed $\delta^{13}C$ signal. SIMS carbon isotope values for organic matter and organic-free siderite are similar to the bulk $\delta^{13}C_{org}$ and $\delta^{13}C_{carb}$ values (−39.0‰ and −6.3‰, respectively), but pyrite sulfur isotope values are significantly higher than bulk values ($\delta^{34}S$ = 1.26; $\Delta^{33}S$ = 2.97‰) for this sample (Kaufman *et al.*, 2007).

Fig. S19). This pyrobitumen was analyzed four times, yielding the highest $\delta^{13}C$ values in the sample ($-39.1 \pm 0.5‰$), and 3.5‰ higher than the average for other organic domains in this sample ($-42.6 \pm 3‰$). In addition to its high $\delta^{13}C$ value, the Jeerinah Fm pyrobitumen nodule is unique in that it is largely bounded by what appear to be detrital grains. Most other organic matter in this sample is texturally homogeneous, also appearing like pyrobitumen, but is typically surrounded by chlorite (Fig. S5) that may be related to a < 2.2 Ga metasomatic overprint (Rasmussen *et al.*, 2005; White *et al.*, 2014a).

Carbonate carbon isotope analysis

As discussed previously, the conversion of inorganic carbon to C^- is a multistep process and inefficient (e.g., ~0.9 MHz ^{12}C/nA/wt.% for calcite standards) relative to production of C^- from organic carbon (~4.7 MHz ^{12}C/nA/wt.% for anthracite standards) during SIMS. This affords the unique ability to accurately analyze the isotopic composition of small organic carbon domains in carbonate matrixes. However, the high relative efficiency of organic carbon ionization presents a challenge for accurate carbon isotope analysis of sedimentary carbonates that have small organic inclusions. In this study, we analyzed 80 targets of calcite and dolomite in seven samples (ABDP-9 111.22 and 148.37; RHDH2a 252.2 and 285.3; WRL-1 289.45 and 520.6; SV-1 55.3) and four siderite targets in one sample (ABDP-9 161.02). In general, achieving accurate individual SIMS analyses of carbonate was impossible due to the presence of organic matter in the analytical region. We used $^{12}C_{rel}$ of each carbonate analysis to assess whether organic inclusions had been analyzed: $^{12}C_{rel} > 1.0$ typically indicated the presence of organic matter. We note that further complexity in ^{12}C count rates can be introduced by the presence of non-carbon bearing (e.g., quartz) inclusions in carbonate, but we suggest based upon our petrographic observations (Fig. S19) that the extent to which this affects our conclusions is minimal, as inclusions of carbon-free minerals are readily detected with SEM and EDS. In some samples, a linear correlation between $\delta^{13}C$ and $^{12}C_{rel}$ was observed, with higher count rates yielding lower $\delta^{13}C$. In these cases, it was possible to estimate a $\delta^{13}C$ value for organic-free carbonate minerals (similar to a bulk value) using the $\delta^{13}C$ value calculated for $^{12}C_{rel} = 100\%$ (an example is shown in Fig. S9). These '$\delta^{13}C_{dol}$ calc' and '$\delta^{13}C_{cal}$ calc' values are shown in Table 3. Further, it was then possible to calculate $\Delta^{13}C_{dol\text{-}org}$ and $\Delta^{13}C_{cal\text{-}org}$ using average SIMS $\delta^{13}C$ of organic matter in the samples.

Primary vs. secondary signals

With the exception of the millimeter-scale calcite vein in the Carawine Dolomite (RHDH2a 252.2) with $\delta^{13}C_{cal}$ calc = 0.5‰, all estimates for $\delta^{13}C$ of carbonate minerals are <0‰. Estimates for dolomite range from −9 to −1.4‰, and for calcite from −18.5 to −7.1‰. The strongly negative $\delta^{13}C$ estimated for most calcites analyzed in this study suggests that they precipitated after deposition in the presence of remineralized organic carbon. It is possible, however, that calcite in sample RHDH2a 252.2 represents a primary phase formed in surface waters and that dolomite formed in sediments in the presence of organic matter. The relative recalcitrance of this early diagenetic dolomite would have led to its survival of the dissolution event that formed the stylolites in this sample.

Assessing metabolic and diagenetic signatures using paired organic and inorganic SIMS carbon isotope analysis

Given the difficulty of accurate SIMS $\delta^{13}C$ analysis of sedimentary carbonate minerals introduced by small organic inclusions (discussed previously), we caution that the data presented here for inorganic carbon are less robust than those for organic carbon and pyrite sulfur. In some cases, however, our SIMS data align well with earlier conventional $\delta^{13}C_{carb}$ data from the same samples, validating the approach we outline here. With these caveats in mind, and because this approach may be useful in future investigations, we present the following as a case study for this technique.

Although the minimum $\delta^{13}C$ of organic matter is quite low (<−40‰) in the majority of samples, RHDH2a 252.2 (Carawine Dolomite) is the only sample for which paired, *in situ* inorganic and organic carbon isotope data from both calcite and dolomite suggest a large (>40‰) $\Delta^{13}C_{carb\text{-}org}$ offset inconsistent with carbon fixation via the Calvin–Benson–Bassham (CBB) reductive pentose phosphate pathways used by photo- and chemo-autotrophs. This is broadly consistent with earlier evidence from bulk $\delta^{13}C$ data (Eigenbrode, 2004; Eigenbrode & Freeman, 2006), strengthens the case for a significant paleoecological role of methanotrophy in the Neoarchean (Hayes, 1983, 1994; Eigenbrode & Freeman, 2006) and provides strong, new evidence for the presence of this metabolism in shallow shelf environments (likely in sediments).

In ABDP-9 111.22 and 148.37, $\Delta^{13}C_{dol\text{-}org}$ is 30.1‰ and 33.2‰, respectively (Table 3). This is self-consistent and agrees with previously reported, paired, bulk inorganic and organic $\delta^{13}C$ data for ABDP-9 111.22 that showed $\Delta^{13}C_{carb\text{-}org} = 30.1‰$ (Kaufman *et al.*, 2007). However, $\Delta^{13}C_{cal\text{-}org}$ is smaller in these samples, 24.4‰ and 23.6‰, respectively (Table 3). An extrapolation of the equilibrium carbon isotope fractionation expression for coexisting metamorphic calcite and dolomite to 20 °C indicates that dolomite is ^{13}C-enriched by 2.4‰ relative to calcite (Sheppard & Schwarcz, 1970). If calcite is a primary carbonate phase in the upper Mount McRae Shale as previously reported by Kaufman *et al.* (2007), and represented a reli-

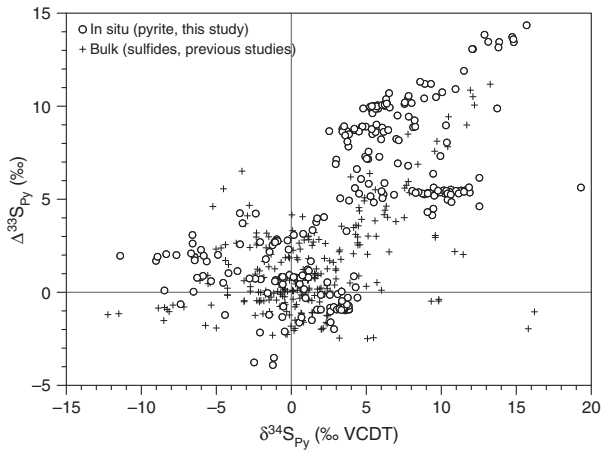

Fig. 8 A comparison of previously compiled bulk sulfur three-isotope data from Neoarchean rocks (Canfield & Farquhar, 2009; Williford *et al.*, 2011) and *in situ* SIMS data from this study. Analytical uncertainty is smaller than the symbols.

able proxy for $\delta^{13}C$ of dissolved inorganic carbon in seawater, then the apparent metabolic fractionation would be ~24‰ (and would indicate that dolomite precipitated out of equilibrium). It is quite possible, however, that the calcite domains reported in this sample are early diagenetic (precipitated in the presence of remineralized organic carbon), and their use in a metabolic proxy is unwarranted.

Three nodule-forming siderite grains were analyzed in ABDP-9 161.02 (Fig. 7), and their $\delta^{13}C$ was determined opportunistically using the atypical method of relative bias correction based upon bracketing analyses of UWC-3 and later analyses of Ivigtut siderite. The three siderite analyses had $^{12}C^-$ count rates ranging from 4.4×10^6 to 6.7×10^7 cps, suggesting that at least two sampled organic carbon inclusions. The analysis with the lowest count rate has $\delta^{13}C = -6.2$‰, remarkably close to the bulk $\delta^{13}C_{carb}$ value for this sample of −6.3‰ in which siderite is the dominant carbonate phase (Kaufman *et al.*, 2007). Kerogen associated with this nodule has $\delta^{13}C = -39.5 \pm 0.5$‰, indicating an apparent metabolic fractionation ($\Delta^{13}C_{sid\text{-}org}$) of 33.5‰. This value is 10‰ greater than that determined for the upper Mount McRae Shale, and together with changes in carbonate mineralogy and sulfur isotope systematics (discussed below), is consistent with strong variability in the expression of microbial metabolisms during the latest Archean.

Sulfur isotope analysis

In three separate analytical sessions during this study, 266 pyrite targets were analyzed for sulfur three-isotopic composition with a ~10-μm-diameter beam. After minimal repolishing to remove analytical pits from sulfur three-isotope analysis, 58 additional pyrite targets were analyzed for sulfur four-isotopic composition using a ~20-μm-diameter beam. Values of $\delta^{34}S$ and $\Delta^{33}S$ measured in this study of 10 samples of <1 cm^2 each encompass nearly the entire range reported in earlier compilations of bulk sulfur three-isotope data from Neoarchean samples (Williford *et al.*, 2011; Canfield & Farquhar, 2009; Fig. 8). This suggests that significant unrecognized variability exists in samples that have previously been analyzed only by bulk techniques, consistent with other SIMS studies of Archean and Proterozoic sulfides (Philippot *et al.*, 2007, 2012; Bontognali *et al.*, 2012; Farquhar *et al.*, 2013; Johnson *et al.*, 2013; Fischer *et al.*, 2014; Zhelezinskaia *et al.*, 2014).

Morphologically correlated sulfur isotopic heterogeneity in the Jeerinah Fm

Of forty pyrite targets analyzed in sample WRL-1 679.9 of the Jeerinah Fm, 32 define a relatively tight field with $\delta^{34}S$ ranging from −0.9‰ to 4.1‰ and $\Delta^{33}S$ from −1.0‰ to 0.9‰ (Fig. 9C). These pyrites occur in agglomerations of euhedral to subhedral crystals whose relatively narrow range of sulfur isotopic compositions is consistent with early diagenetic formation in sediments from (either abiotic or microbial) sulfate reduction. In the same sample, another group of 8 targets defines a linear array with a larger range of mass-dependent ($\delta^{34}S$ from 4.0‰ to 13.4‰) and mass-independent ($\Delta^{33}S$ from 4.8‰ to 9.9‰) fractionation (Fig. 9). This more isotopically heterogeneous group of pyrites generally occurs as isolated, individual grains within the clastic matrix, sometimes with rounded margins, suggestive of a detrital component in this sample. The large range in $\delta^{34}S$ coupled with strongly positive S-MIF suggests metabolic recycling of sulfur (disproportionation followed by sulfate reduction) that left the atmosphere as S^0 (Pavlov & Kasting, 2002; Ono *et al.*, 2003; Kaufman *et al.*, 2007). However, the rounded grain morphologies (that may indicate a detrital component) suggest that this record of the sulfur cycle may predate the deposition of the host rock.

The roughly time-equivalent sample of the Jeerinah Fm from the RHDH2a core (285.3) shows a similar separation in sulfur isotopic compositions (Fig. 9B), with one small group of six pyrite targets having $\delta^{34}S$ between −0.8‰ and 1.8‰ and $\Delta^{33}S$ between 0.8‰ and 4.0‰ and a larger group defining a linear array with $\delta^{34}S$ from 2.2‰ to 15.3‰ and $\Delta^{33}S$ from 6.9‰ to 14.4‰ (Fig. 9). The petrographic difference between these two groups of Jeerinah Fm pyrite in the RHDH2a sample is not as clear as they are for WRL-1. Pyrite targets in RHDH2a 285.3 are generally relatively large (10s to >100 μm), commonly subangular to partially rounded, and associated with pyrobitumen and Fe- and Mg-bearing chlorite.

Intriguingly, the sample of the Jeerinah Fm (RHDH2a 285.3) interpreted to have been deposited closer to the basin margin is dominated by pyrite with diverse sulfur iso-

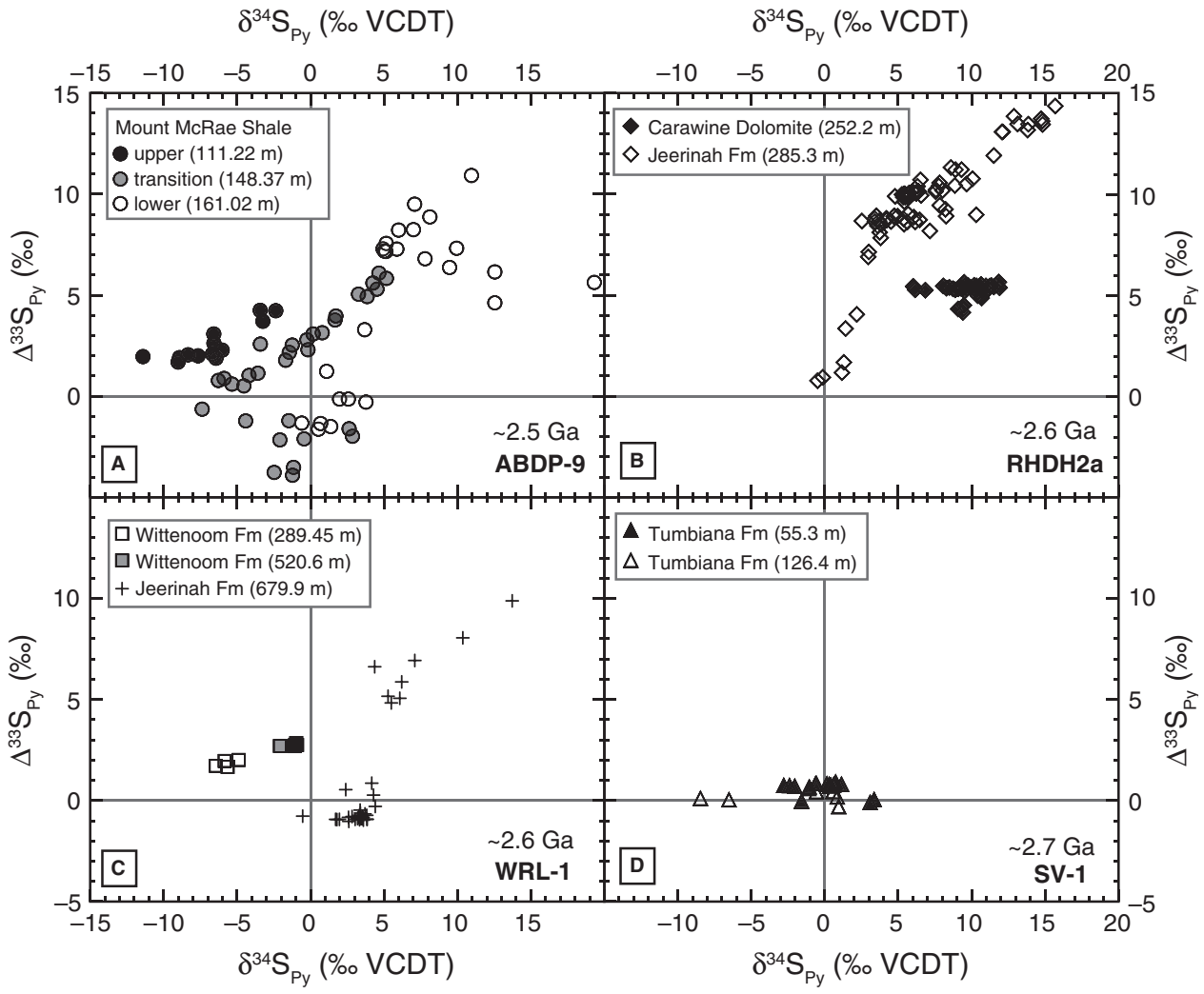

Fig. 9 Sulfur three-isotope data from this study shown for individual samples in ABDP-9 (A), RHDH2a (B), WRL-1 (C), and SV-1 (D) drill cores. External precision is smaller than symbols.

topic compositions distributed along a linear array of mostly positive $\Delta^{33}S$ and $\delta^{34}S$, whereas the sample from the depocenter (WRL-1 679.9) is dominated by pyrite with $\Delta^{33}S$ and $\delta^{34}S$ closer to zero. It may be that this latter variety of pyrite (with near-zero $\Delta^{33}S$ and $\delta^{34}S$) represents relatively strong sulfate limitation in the depocenter, whereas the former variety of pyrite (with wide-ranging $\Delta^{33}S$ and $\delta^{34}S$) represents conditions of sulfur cycling restricted to the margin (e.g., metabolic recycling with less sulfate limitation). If so, then pyrite in WRL-1 679.9 with $\Delta^{33}S$ and $\delta^{34}S \geq 5‰$ may indeed be detrital, having washed into deeper water from the basin margin—consistent with our petrographic observations.

Previous $\delta^{34}S$ measurements of Jeerinah Fm pyrite using laser ablation showed 6–7‰ mm-scale heterogeneity, interpreted as strong evidence for microbial sulfate reduction (Kakegawa *et al.*, 2000; Kakegawa & Nanri, 2006). The sample of the Jeerinah Fm analyzed in this study exhibits even larger, micrometer-scale heterogeneities in $\delta^{34}S$, $\Delta^{33}S$, and $\Delta^{36}S$ (e.g., RHDH2a 285.3#16 and #19; Fig. S19). Over a distance of ~20 μm, from the core of target RHDH2a 285.3#16 to the rim, $\delta^{34}S$ increases by 6.2‰ (from 3.5 to 9.7 ± 0.4‰, 2SD) and $\Delta^{33}S$ increases by 3‰ (from 7.8 to 10.8 ± 0.09‰, 2SD). Another target (#19) in the same sample (RHDH2a 285.3) shows differences of 12.7‰ (2.6–15.3 ± 0.5‰, 2SD) in $\delta^{34}S$, 7.5‰ (6.9–14.4 ± 0.06‰, 2SD) in $\Delta^{33}S$, and −5.5‰ (−5.8 to −11.3 ± 0.9‰, 2SD) in $\Delta^{36}S$ over only a distance of only ~40 μm. Not only is this pyrite grain extremely heterogeneous, it exhibits the largest S-MIF yet reported from any rock (Philippot *et al.*, 2012). Although much larger gradients in $\delta^{34}S$ (>30‰) have been observed at smaller (<4 μm) spatial scales using the extremely high spatial resolution SIMS techniques we reported in an earlier study of

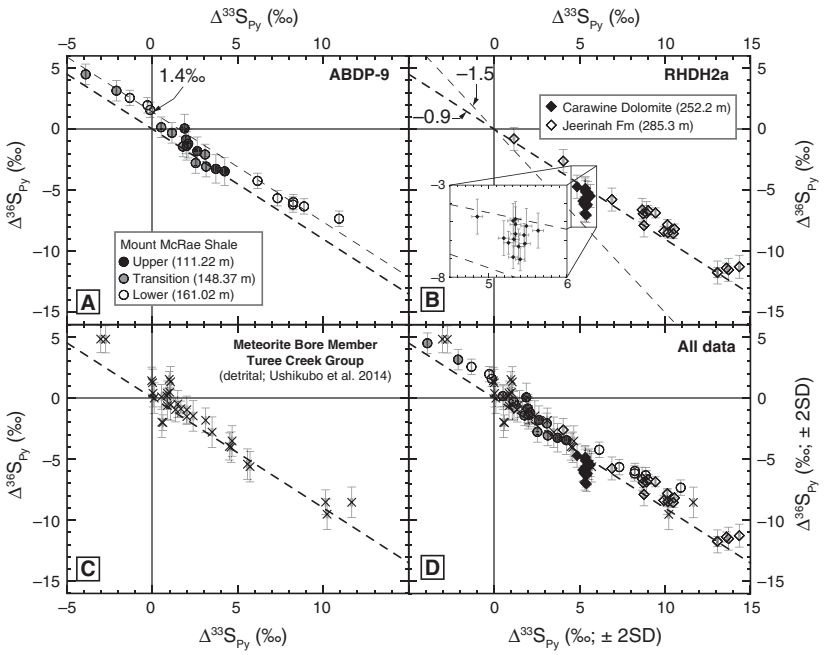

Fig. 10 Sulfur four-isotope data from this study shown for individual samples in ABDP-9 (A) and RHDH2a (B) drill cores, outcrop samples from ~2.4 Ga Meteorite Bore member, Kungarra Fm (C; Ushikubo *et al.*, 2014), and all samples analyzed in this study (D). Dashed line in all panels represents the 'Archean array' with slope of −0.9 and intercept of 0. Secondary dashed line in (A) shows best linear fit to ABDP-9 data, with intercept of 1.4‰. Secondary dashed line in (B) indicates a shifted array previously hypothesized to result from an intermittent atmospheric 'organic haze' between 2.65 and 2.5 Ga (Zerkle *et al.*, 2012). Inset in (B) shows data from RHDH2a 252.2 m (Carawine Dolomite) that depart from the −0.9 array. Error bars show ±2SD external precision.

Paleoproterozoic pyrite (Williford *et al.*, 2011), to our knowledge the gradients in $\Delta^{33}S$ and $\Delta^{36}S$ we report here for the Jeerinah Fm are the largest so far observed.

Isotopic relations correlated with magnetic anomalies, but otherwise similar to those we report from the Jeerinah Fm, have recently been reported from Archean pyrite nodules in the Barberton Greenstone Belt using scanning high-resolution superconducting magnetic (SQUID) microscopy SQUID-SIMS, and these were interpreted to have resulted from dynamic mixing of locally heterogeneous and compositionally evolving sulfur sources, and metasomatic alteration (including pyrite to pyrrhotite transformations indicated by magnetic domains in pyrite) that postdated deposition by hundreds of Myr (Fischer *et al.*, 2014). Although the resolution of the SQUID-SIMS technique (50-μm SQUID step size, ~25-μm SIMS analytical area) reported by Fischer *et al.* (2014) is insufficient to assess whether the isotopic heterogeneities reported here (e.g., over scales of ~20 μm in a ~50-μm grain) are associated with magnetic anomalies, we suggest that some of the variability we observe may be driven by similar mechanisms to those hypothesized in that study. Similarly, distinction of zonation of minor elements in pyrite (e.g., As, Ni, Co) by electron probe microanalysis (EPMA) can be achieved with a lateral resolution on the micrometer scale. This method, coupled to SIMS, has been used to distinguish multiple generations of pyrite with correlated elemental and isotopic heterogeneities in individual grains (Williford *et al.*, 2011) and nodules (Marin-Carbonne *et al.*, 2014).

Accordingly, we apply extraordinary care in target selection and analysis in order to understand the degree to which post-depositional processes have affected our samples. To assess the confidence with which we have identified our sulfur isotope analysis targets as pyrite, we analyzed pyrite and pyrrhotite standards by EDS. Although EDS does not provide the accuracy in atom% associated with wavelength-dispersive spectroscopy (e.g., with EPMA), pyrite and pyrrhotite are quickly and clearly distinguishable by their relative Fe and S peak heights using this technique. At 15 keV, the S/Fe peak height ratio is typically 4 for pyrite and 2 for pyrrhotite. We find no evidence of pyrite to pyrrhotite transformations in the analytical targets reported here.

Associations between pyrite, pyrobitumen, and chlorite in the Jeerinah Fm suggest that thermochemical sulfate reduction associated with metamorphism/metasomatism may have played at least a secondary role in pyrite formation; that is, a 'primary' episode of early diagenetic, microbial sulfate reduction may have been followed by a later (perhaps by 100s of Myr), 'secondary' episode of abiotic sulfate reduction accompanied by evolution of pyrobitumen from kerogen and metamorphic chlorite transformations. Indeed, anomalous sulfur isotope fractionation effects completely decoupled from atmospheric chemistry – such as those observed in laboratory experiments with thermochemical sulfate reduction (Lasaga *et al.*, 2008; Watanabe *et al.*, 2009) – may explain *some* of the intragrain heterogeneity reported here. Partial dissolution, remobilization, and local redeposition could also have contributed to these heterogeneities, although we find no evidence for introduction of secondary minor elements (e.g., Ni, Co, As) during late diagenesis as has been reported for other sedimentary pyrite with strong sulfur isotope zonation (Williford *et al.*, 2011).

Atmospheric and metabolic effects on sulfur isotope systematics

Pyrite grains in the oldest samples analyzed in this study, from the ~2.7 Ga Tumbiana Fm, have universally negative $\delta^{34}S$, as low as −9‰, but they show very little heterogeneity in $\Delta^{33}S$ (−0.3 to 0.9‰). This is consistent with previous bulk sulfur isotope analysis of pyrite in the Tumbiana Fm (Thomazo *et al.*, 2009a) and the Manjeri and Chershire Fms of Zimbabwe (Thomazo *et al.*, 2013), and indicates that the dampened S-MIF characteristic of the Mesoarchean (Farquhar *et al.*, 2007b) persisted into the early Neoarchean. Organic matter in samples of the Tumbiana Fm with $\delta^{13}C$ as low as −52.4‰ supports the earlier contention that methanotrophy may have played a role in the relatively small range of S-MIF observed between ~3.2 and 2.7 Ga, and below we discuss similarly coupled carbon and sulfur isotope systematics evident in the younger Neoarchean record from Australia.

Slopes of linear $\Delta^{33}S/\delta^{34}S$ arrays for Jeerinah Fm pyrite targets in the WRL-1 (depocenter) and RHDH2a (marginal) are indistinguishable (0.5; Fig. 9), but the $\Delta^{33}S$ intercept is higher (6.9) for RHDH2a pyrites compared to WRL-1 pyrite (3.1). We interpret the similar slope to indicate stability of atmospheric MIF-S production (on a ~10 Myr time scale) during the deposition of the Jeerinah Fm. The mechanism behind the different intercepts is more difficult to understand in the depositional context. A higher $\Delta^{33}S$ intercept suggests an increased role of S^0 relative to SO_4^{2-} in the formation of the RHDH2a Jeerinah pyrite compared to the WRL-1 pyrite. This conclusion is based upon a model of S-MIF production in which positive $\Delta^{33}S$ is carried from the atmosphere to the ocean by elemental sulfur, and negative $\Delta^{33}S$ by sulfate (Pavlov & Kasting, 2002; Ono *et al.*, 2003).

Sulfur four-isotope compositions in the Carawine Dolomite (RHDH2a 252.2; Fig. 10B) depart from the $\Delta^{36}S/\Delta^{33}S$ array observed for other samples in this study (and previous studies; (e.g., Farquhar *et al.*, 2000; Ono *et al.*, 2003). Intriguingly, organic matter in this sample of the Carawine Dolomite has lower typical $\delta^{13}C$ than any other sample in this study (avg. −49.5‰), adding to the growing body of evidence for a connection between methane and S-MIF. Rotation of the $\Delta^{36}S/\Delta^{33}S$ array away from a typical slope of −0.9 toward a slope of −1.5 has been interpreted as evidence for changing atmospheric production of S-MIF, with an 'organic haze' as the hypothesized mechanism (Domagal-Goldman *et al.*, 2008; Thomazo *et al.*, 2009a; Zerkle *et al.*, 2012; Farquhar *et al.*, 2013). Zerkle *et al.* (2012) defined the $\Delta^{36}S/\Delta^{33}S_{dev}$[3] index to describe this behavior, and using bulk measurements, found that the greatest deviation ($\Delta^{36}S/\Delta^{33}S_{dev} \geq 2$) occurred in samples with $\delta^{13}C_{org} < -40‰$. A subset of the samples analyzed in bulk by Zerkle *et al.* (2012) were analyzed by Farquhar *et al.* (2013) for sulfur four isotopes using the same instrument (CAMECA IMS 1280) as we used in this study, but in a different laboratory with different analytical conditions (e.g., electron multiplier rather than Faraday cup detector for ^{36}S). These *in situ* data were consistent with the findings of Zerkle *et al.* (2012), and the authors further argued for two distinct pathways of Archean pyrite formation (see below; Farquhar *et al.*, 2013).

Samples analyzed in this study with the lowest $\delta^{13}C$ values of organic matter (and average $\delta^{13}C$ of organic matter <40‰; Table 3), including the Carawine Dolomite, Jeerinah Fm, and the lowest sample of the Mount McRae Shale, also exhibit the highest values of $\Delta^{36}S/\Delta^{33}S_{dev}$ (as high as 2.2, 1.7, and 2.5, respectively; supplementary data). Sulfur isotope data from the Carawine Dolomite depart from the Archean array with (loose) linearity. Similar systematics have been observed in Phanerozoic fossils preserved by pyritization of organic matter (Ono *et al.*, 2006). Accordingly, the departure from the Archean $\Delta^{36}S/\Delta^{33}S$ array observed in the Carawine Dolomite could result from mass-dependent effects expressed through reaction networks associated with microbial sulfur metabolism (Farquhar *et al.*, 2003, 2007a; Johnston *et al.*, 2007, 2008; Zerkle *et al.*, 2010). Archaeal anaerobic methanotrophy (ANME) and bacterial sulfate reduction are coupled by consortia in modern ecosystems (Orphan *et al.*, 2001a,b), and the data presented here may indicate a similar connection between these organisms in the Neoarchean as recently proposed by Thomazo *et al.* (2013).

Sulfur isotope systematics in the ~2.5 Ga Mount McRae Shale

Multiple lines of geochemical evidence from samples of the Mount McRae Shale recovered from the ABDP-9 core, including sulfur three-isotope measurements, were used to argue for oxygenation in the surface ocean (Anbar *et al.*, 2007; Kaufman *et al.*, 2007). In particular, a major transition from pyrite with uniformly positive $\delta^{34}S$ and $\Delta^{33}S$ below 153 m in the ABDP-9 core to pyrite with negative $\delta^{34}S$ and positive $\Delta^{33}S$ was interpreted to represent emergence of an oxidative sulfur cycle, and a shorter interval between 153 and 135 m with negative values of both $\delta^{34}S$ and $\Delta^{33}S$ was interpreted to represent increasing seawater sulfate concentrations due to oxidative weathering (Kaufman *et al.*, 2007).

In multiple analyses of pyrite from only three samples, we observe the entire range of sulfur isotopic heterogeneity so far detected by bulk analysis in the ABDP-9 core (Figs. 9 and 10). Our data are broadly consistent with the earlier bulk measurements and interpretations of the sulfur

[3] $\Delta^{36}S/\Delta^{33}S_{dev} = |\Delta^{36}S/\Delta^{33}S_{ref} \times \Delta^{33}S_{sample} - \Delta^{36}S_{sample}|$ with $\Delta^{36}S/\Delta^{33}S_{ref} = -0.9$.

Table 4 SIMS sulfur isotope data from ten Neoarchean rock samples

				$\delta^{34}S$ (‰ VCDT)			$\Delta^{33}S$ (‰)				$\Delta^{36}S$ (‰)			
Core	Depth (m)	Unit	Est. Age (Ma)	Max	Min	Avg	Max	Min	Avg	*n*	Max	Min	Avg	*n*
ABDP-9	111.22	Mount McRae	2500	−2.7	−11.8	−7.0	4.3	1.7	2.6	13	0.6	−3.5	−1.7	7
ABDP-9	148.37	Mount McRae	2500	4.8	−7.7	−1.1	6.1	−3.9	1.4	32	4.5	−3.1	0.2	8
ABDP-9	161.02	Mount McRae	2500	18.7	−0.9	5.7	10.9	−1.6	4.7	25	2.6	−7.3	−3.3	9
WRL1	289.45	Wittenoom	2577	−5.2	−6.8	−6.0	2.0	1.7	1.8	4	n.d.	n.d.	n.d.	n.d.
WRL1	520.6	Wittenoom	2596	−1.3	−2.4	−1.5	2.9	2.7	2.7	6	n.d.	n.d.	n.d.	n.d.
WRL1	659.55	Marra Mamba	2629	n.d.	n.d.	n.d.	n.d.	n.d.	n.d.	n.d.	n.d.	n.d.	n.d.	n.d.
WRL1	679.9	Jeerinah	2632	13.4	−0.9	3.7	9.9	−1.0	0.8	40	n.d.	n.d.	n.d.	n.d.
RHDH2a	252.2	Carawine	2633	11.5	5.2	9.3	5.6	4.1	5.3	45	−4.7	−7.0	−5.7	15
RHDH2a	285.3	Jeerinah	2639	15.3	−0.8	6.3	14.4	0.8	9.4	76	−0.8	−11.7	−7.8	19
SV1	55.3	Tumbiana	2721	3.0	−3.3	0.3	0.9	−0.1	0.6	18	n.d.	n.d.	n.d.	n.d.
SV1	126.4	Tumbiana	2725	0.6	−8.8	−2.4	0.6	−0.3	0.2	7	n.d.	n.d.	n.d.	n.d.

isotopic composition of pyrite in the Mount McRae Shale (Ono *et al.*, 2003; Kaufman *et al.*, 2007), but the high spatial resolution, *in situ* nature of our analysis, and the addition of $\Delta^{36}S$ measurements offer powerful new windows into the biogeochemistry of this unit. In the oldest sample, taken 8 m below the '153 m transition' (161.02 m), $\delta^{34}S$ varies from −0.9 to 18.7‰, $\Delta^{33}S$ from −1.6 to 10.9‰, and $\Delta^{36}S$ from −7.3 to 2.6‰. The range in $\delta^{34}S$ and $\Delta^{33}S$ encompasses the range reported from bulk measurements below 153 m in the ABDP-9 core. Pyrite in this sample exhibits strong linearity in $\Delta^{36}S/\Delta^{33}S$ ($r^2 = 0.99$), with a slope of −0.9, typical for the Archean ($\Delta^{36}S = -0.88*\Delta^{33}S + 1.39$; Fig. 10A). A shift in the $\Delta^{36}S$ intercept in the $\Delta^{36}S/\Delta^{33}S$ array to 1.4‰ can be driven by changing fractionation during sulfate reduction (Ono *et al.*, 2006), but increasing fractionation would tend to shift the intercept in the negative direction (Zerkle *et al.*, 2012). Values of $\delta^{34}S$ are high, and almost uniformly positive, implying low seawater sulfate concentration and a greater relative contribution of elemental sulfur (by way of polysulfide intermediates; (Farquhar *et al.*, 2013) than sulfate to pyrite formation.

Of nine targets in ABDP-9 161.02 chosen for sulfur four-isotope analysis, eight have $\Delta^{36}S/\Delta^{33}S_{dev}$ >1.2, and one has $\Delta^{36}S/\Delta^{33}S_{dev} = 2.5$, comparable to the high values observed in the a Upper Nauga Fm, similar in age (~2.5 Ga) to the Mount McRae Shale (Zerkle *et al.*, 2012). Values of $\Delta^{36}S/\Delta^{33}S_{dev}$ vary from 0.9 to 2.5 (with an average of 1.5), and this sample also has the lowest $\delta^{13}C$ (−42.2‰) recorded in the ABDP-9 core. Critically, however, the slope of the $\Delta^{36}S/\Delta^{33}S$ array in this sample is not rotated from typical Archean values, but 'anomalous' $\Delta^{36}S/\Delta^{33}S_{dev}$ values are driven by a change in $\Delta^{36}S$ intercept.

Target 23 in ABDP-9 161.02 exhibits a large gradient from the interior to the exterior of the nodule: the interior has $\delta^{34}S = 0.5$‰ and $\Delta^{33}S = 1.2$‰, whereas the exterior has $\delta^{34}S = 9.6$‰ and $\Delta^{33}S = 7.3$‰ (Fig. S19). Only the exterior of the nodule (exposed by repolishing the sample between sulfur three- and four-isotope analysis sessions) was analyzed for $\Delta^{36}S$, so we do not know whether or not a gradient also exists for $\Delta^{36}S/\Delta^{33}S$ in this target. The large (9‰) gradient in $\delta^{34}S$, distributed over only a few micrometer, suggests Rayleigh fractionation during formation of the nodule.

A recent and detailed petrographic and geochemical analysis of nodular associations of organic matter, pyrite, and siderite in Mississippian shales from Wardie, Scotland (Bojanowski & Clarkson, 2012), reports textures similar to those we observe in ABDP-9 161.02 (see especially Fig. 4 in that publication). Based upon $\delta^{13}C$ values in siderite >5‰, as well as organic matter associations, these authors suggest that the precipitation of Wardie siderite relied on alkalinity produced during methanogenesis, initiated in the sulfate reduction zone after rapid consumption of sulfate. We propose a similar mechanism: microbial sulfate reduction proceeded under low sulfate concentrations typical of Archean seawater until sulfate was exhausted, at which point methanogenesis and dissimilatory iron reduction provided the conditions required for siderite formation. This is consistent with the gradient we observe in $\delta^{34}S$, but it does not immediately explain the gradient in $\Delta^{33}S$ from the core to rim of a nodule, observed, for example, in ABDP-9 161.02 target 23 (Fig. S19). Such a gradient, similar to those observed in larger pyrite nodules of Archean age (Fischer *et al.*, 2014; Marin-Carbonne *et al.*, 2014), requires local heterogeneities in $\Delta^{33}S$ of pore fluids, changes in S-MIF production on the time scale of nodule growth, or an as yet unconstrained biological effect.

The model proposed by Farquhar *et al.* (2013) suggests two distinct pathways for pyrite formation that depend upon sulfate availability, and that the relative contribution of these pathways determines the final $\Delta^{33}S$ of pyrite: when the 'direct' reaction of relatively abundant and soluble sulfate (e.g., from an atmospheric exit channel as H_2SO_4 with

negative $\Delta^{33}S$) with sulfide dominates, pyrite with low $\Delta^{33}S$ is produced. When the 'indirect' reaction of insoluble elemental sulfur (e.g., from an atmospheric exit channel as S_8 with positive $\Delta^{33}S$) with sulfide dominates, soluble polysulfide intermediates with high $\Delta^{33}S$ are produced and impart this signature to later formed pyrite. We further suggest here the logical extension of this argument, that changing relative expression of these two pathways in closed system conditions could result in a positive gradient in $\Delta^{33}S$ within a growing grain or nodule as a local reservoir of low $\Delta^{33}S$ sulfate is depleted and the relative dominance of high $\Delta^{33}S$ polysulfide intermediates in pyrite formation increases.

In the 'transition' sample, taken from 148.37 m in the ABDP-9 core, $\delta^{34}S$ varies from −7.7 to 4.8‰, $\Delta^{33}S$ from −3.9 to 6.1‰, and $\Delta^{36}S$ from −3.1 to 4.5‰. In the youngest sample (111.22 m), $\delta^{34}S$ is universally negative, varying from −11.8 to −2.7‰, whereas $\Delta^{33}S$ is positive from 1.7 to 4.3‰, and $\Delta^{36}S$ varies from −3.5 to 0.6‰ (Table 4, Figs 9A, 10A). Decreasing values of $\delta^{34}S$ in these three samples of the ABDP-9 core, as well as decreasing trends in $\Delta^{33}S$, are consistent with a secular increase in seawater sulfate during deposition of the Mount McRae Shale, perhaps due to oxidative continental weathering as previously proposed by Kaufman *et al.* (2007). Pyrite grains from the two younger samples of the Mount McRae Shale, from 148.37 and 111.22 m in the ABDP-9 core, have $\Delta^{36}S/\Delta^{33}S_{dev}$ values that are significantly lower than grains in the oldest sample (avg. = 0.7 vs. 1.5; $P < 0.02$ in a two-tailed Student's t-test), but the populations from the two younger samples are statistically indistinguishable from each other (supplementary data). This is consistent with a transition in the expression of $\Delta^{36}S/\Delta^{33}S$ at 153 m depth in the core (Kaufman *et al.*, 2007). Indeed, $\Delta^{36}S/\Delta^{33}S$ relations for individual pyrite grains in all three samples of the Mount McRae Shale analyzed in this study are strongly linear (r^2 from 0.89 to 0.99), and slopes decrease from −0.88 (161.02 m) to −1.07 (148.37 m) to −1.26 (111.22 m).

Finally, two distinct populations of pyrite with distinct sulfur isotope systematics were observed in ABDP-9 148.37 (Fig. S8). Some pyrite targets (e.g., ABDP-9 148.37a targets 11 and 14) are distinguished by their nodular occurrence in intimate association with a rim of chlorite and sometimes calcite. Other pyrite in the sample is not associated with chlorite, and commonly has rounded and/or broken margins, consistent with a detrital origin. Chlorite-associated pyrite has higher $\delta^{34}S$ and $\Delta^{33}S$ (>0‰) than non-chlorite-associated pyrite. The original sulfur source would have left the atmosphere as zero valent, elemental sulfur, requiring multiple metabolic pathways to pyrite formation including disproportionation and sulfate reduction.

CONCLUSIONS

Spatially resolved, *in situ* carbon and sulfur isotope analysis of organic matter, carbonate minerals, and pyrite, supported by light and electron microscopy as well as elemental mapping deepen our understanding of Neoarchean biogeochemistry. The approach described here offers an unprecedented combination of spatial resolution, precision and accuracy for carbon and sulfur isotope analysis of micrometer-scale domains of sedimentary organic matter, carbonate minerals, and pyrite, and maximizes potential information recovery in sample limited scenarios (such as scientific drilling or Mars sample return, e.g.). Although SIMS analysis yields extraordinary information density when done correctly, it is labor intensive relative to conventional, or 'bulk' analysis. For this reason, and also because of the inherent sampling biases that can be associated with resolution-limited spatially resolved techniques, a combination of *in situ* and bulk analysis (when sample sizes permit) is the best approach to maximize information recovery. As was the case for this study, bulk analysis is particularly useful to guide the selection of samples to analyze in greater detail. Key findings are as follows:

1 A new method for the simultaneous collection of $^{13}CH/^{13}C$ data, along with a new set of organic standards that can be used to correct for the H/C effect is described. Based upon the data we report here and the earlier reports from another laboratory, we conclude that a failure to account for this effect can lead to inaccuracy of up to 4‰.
2 This new method for SIMS $\delta^{13}C$ analysis of organic matter affords reproducibilities of 0.3‰ routinely (2SD; comparable to bulk analysis by continuous flow techniques) with a 6-μm-diameter beam and 0.8‰ (2SD) with a 1- to 3-μm-diameter beam. The sample volume consumed by each SIMS $\delta^{13}C$ analysis with a 6-μm-diameter beam (~24 μm^3) is ~10^{-5} that typically required for conventional analysis by continuous flow techniques.
3 We have demonstrated $\delta^{13}C$ measurements with subpermil accuracy at count rates as low as 30% of the bracketing standard (i.e., >50% carbonate) due in part to the low conversion of inorganic carbon to C^- anions, relative to organic carbon. Conversely, SIMS $\delta^{13}C$ analyses of sedimentary carbonates are strongly affected by small organic inclusions although correlations between ^{12}C count rate and $\delta^{13}C$ can be used to estimate $\delta^{13}C$ of carbonates in a given sample.
4 The remarkable consistency of averaged SIMS data and earlier bulk data from other laboratories bolsters earlier interpretations of biogeochemical changes observed in Neoarchean drill core material from Australia, including evidence for biotic and abiotic oxidative processes at least 100 Ma prior to the Great Oxidation Event. Fur-

thermore, this consistency lends confidence to the fidelity of the analytical techniques reported here.

5 *In situ* textural and organic carbon isotope evidence for multiple microbial metabolisms, including photoautotrophy and methanotrophy, is preserved at the millimeter scale in a single sample of the ~2.7 Ga Tumbiana Fm.

6 Pyrobitumen nodules in samples of the Jeerinah Fm and Mount McRae Shale are enriched in ^{13}C relative to co-occurring kerogen, and associations with uraniferous minerals suggest that this may be due to radiolytic alteration.

7 Coupled, *in situ* carbon and sulfur isotope analysis of organic matter and pyrite in the ~2.7 Ga Tumbiana Fm are consistent with earlier reports of correlations between low $\delta^{13}C$ organic matter and a dampened S-MIF signal, possibly driven by the temporary accumulation of an organic haze. In the ~2.6 Ga Jeerinah Fm and Carawine Dolomite, the range of S-MIF expanded considerably, but anomalous behavior of the minor sulfur isotopes (^{33}S and ^{36}S) at the scale of individual pyrite grains is associated with extremely low $\delta^{13}C$ of organic matter in intimate association with the pyrite. These strong ties between carbon and sulfur cycling demonstrated for the first time *in situ*, *at the microbial scale*, likely continued through the entire Neoarchean.

ACKNOWLEDGMENTS

We acknowledge Noriko Kita, Jim Kern, John Fournelle, Brian Hess, and H.B. Palomo for their essential contributions to this work. Helpful comments by the editors and three anonymous reviewers improved the quality of this manuscript. Major funding for this study came from the National Aeronautics and Space Administration Astrobiology Institute (NAI). WiscSIMS is partly supported by NSF-EAR-1053466, -1355590. Work at MIT was supported by the Agouron Institute, the NASA Astrobiology Institute and the Simons Foundation Origins of Life Collaboration. Part of this research was done at the Jet Propulsion Laboratory, California Institute of Technology, under a grant from the National Aeronautics and Space Administration. KHW and RES serve on the editorial board of *Geobiology*.

REFERENCES

Anbar AD, Duan Y, Lyons TW, Arnold GL, Kendall B, Creaser RA, Kaufman AJ, Gordon GW, Scott C, Garvin J, Buick R (2007) A whiff of oxygen before the Great Oxidation Event? *Science* **317**, 1903–1906.

Bekker A, Holland HD, Wang PL, Rumble D, Stein HJ, Hannah JL, Coetzee LL, Beukes NJ (2004) Dating the rise of atmospheric oxygen. *Nature* **427**, 117–120.

Blake TS, Buick R, Brown SJA, Barley ME (2004) Geochronology of a Late Archaean flood basalt province in the Pilbara Craton, Australia: constraints on basin evolution, volcanic and sedimentary accumulation, and continental drift rates. *Precambrian Research* **133**, 143–173.

Bojanowski MJ, Clarkson ENK (2012) Origin of siderite concretions in microenvironments of methanogenesis developed in a sulfate reduction zone: an exception or a rule? *Journal of Sedimentary Research* **82**, 585–598.

Bontognali TRR, Sessions AL, Allwood AC, Fischer WW, Grotzinger JP, Summons RE, Eiler JM (2012) Sulfur isotopes of organic matter preserved in 3.45-billion-year-old stromatolites reveal microbial metabolism. *Proceedings of the National Academy of Sciences of the United States of America* **109**, 15146–15151.

Brocks JJ, Logan GA, Buick R, Summons RE (1999) Archean molecular fossils and the early rise of eukaryotes. *Science* **285**, 1033–1036.

Brocks JJ, Buick R, Logan GA, Summons RE (2003a) Composition and syngeneity of molecular fossils from the 2.78 to 2.45 billion-year-old Mount Bruce Supergroup, Pilbara Craton, Western Australia. *Geochimica et Cosmochimica Acta* **67**, 4289–4319.

Brocks JJ, Buick R, Summons RE, Logan GA (2003b) A reconstruction of Archean biological diversity based on molecular fossils from the 2.78 to 2.45 billion-year-old Mount Bruce Supergroup, Hamersley Basin, Western Australia. *Geochimica et Cosmochimica Acta*, **67**, 4321–4335.

Brocks JJ, Love GD, Snape CE, Logan GA, Summons RE, Buick R (2003c) Release of bound aromatic hydrocarbons from late Archean and Mesoproterozoic kerogens via hydropyrolysis. *Geochimica Et Cosmochimica Acta* **67**, 1521–1530.

Buseck PR, Galdobina LP, Kovalevski VV, Rozhkova NN, Valley JW, Zaidenberg AZ (1997) Shungites: the C-rich rocks of Karelia, Russia. *Canadian Mineralogist* **35**, 1363–1378.

Canfield DE, Farquhar J (2009) Animal evolution, bioturbation, and the sulfate concentration of the oceans. *Proceedings of the National Academy of Sciences of the United States of America* **106**, 8123–8127.

Czaja AD, Johnson CM, Beard BL, Eigenbrode JL, Freeman KH, Yamaguchi KE (2010) Iron and carbon isotope evidence for ecosystem and environmental diversity in the similar to 2.7 to 2.5 Ga Hamersley Province, Western Australia. *Earth and Planetary Science Letters* **292**, 170–180.

Des Marais DJ (2001) Isotopic evolution of the biogeochemical carbon cycle during the Precambrian. In: *Stable Isotope Geochemistry*, vol. 43 (eds Valley JW, Cole DR). Mineralogical Society of America, Chantilly, VA, pp. 555–578.

Domagal-Goldman SD, Kasting JF, Johnston DT, Farquhar J (2008) Organic haze, glaciations and multiple sulfur isotopes in the Mid-Archean Era. *Earth and Planetary Science Letters* **269**, 29–40.

Eigenbrode JL (2004) Late Archean microbial ecology: an integration of molecular, isotopic, and lithologic studies. Ph.D. Thesis *Geosciences*. Pennsylvania State University, University Park, PA, 326 pp.

Eigenbrode JL, Freeman KH (2006) Late Archean rise of aerobic microbial ecosystems. *Proceedings of the National Academy of Sciences of the United States of America* **103**, 15759–15764.

Eigenbrode JL, Freeman KH, Summons RE (2008) Methylhopane biomarker hydrocarbons in Hamersley Province sediments provide evidence for Neoarchean aerobiosis. *Earth and Planetary Science Letters* **273**, 323–331.

Eiler JM (2011) Paleoclimate reconstruction using carbonate clumped isotope thermometry. *Quaternary Science Reviews* **30**, 3575–3588.

Farquhar J, Wing BA (2003) Multiple sulfur isotopes and the evolution of the atmosphere. *Earth and Planetary Science Letters* **213**, 1–13.

Farquhar J, Bao HM, Thiemens M (2000) Atmospheric influence of Earth's earliest sulfur cycle. *Science* **289**, 756–758.

Farquhar J, Johnston DT, Wing BA, Habicht KS, Canfield DE, Airieau S, Thiemens MH (2003) Multiple sulphur isotopic interpretations of biosynthetic pathways: implications for biological signatures in the sulphur isotope record. *Geobiology* **1**, 27–36.

Farquhar J, Johnston DT, Wing BA (2007a) Implications of conservation of mass effects on mass-dependent isotope fractionations: Influence of network structure on sulfur isotope phase space of dissimilatory sulfate reduction. *Geochimica Et Cosmochimica Acta* **71**, 5862–5875.

Farquhar J, Peters M, Johnston DT, Strauss H, Masterson A, Wiechert U, Kaufman AJ (2007b) Isotopic evidence for Mesoarchaean anoxia and changing atmospheric sulphur chemistry. *Nature* **449**, 706–U705.

Farquhar J, Cliff J, Zerkle AL, Kamyshny A, Poulton SW, Claire M, Adams D, Harms B (2013) Pathways for Neoarchean pyrite formation constrained by mass-independent sulfur isotopes. *Proceedings of the National Academy of Sciences of the United States of America* **110**, 17638–17643.

Ferry JM, Ushikubo T, Kita NT, Valley JW (2010) Assessment of grain-scale homogeneity and equilibration of carbon and oxygen isotope compositions of minerals in carbonate-bearing metamorphic rocks by ion microprobe. *Geochimica Et Cosmochimica Acta* **74**, 6517–6540.

Fischer WW, Fike DA, Johnson JE, Raub TD, Guan YB, Kirschvink JL, Eiler JM (2014) SQUID-SIMS is a useful approach to uncover primary signals in the Archean sulfur cycle. *Proceedings of the National Academy of Sciences of the United States of America* **111**, 5468–5473.

Fletcher IR, Kilburn MR, Rasmussen B (2008) NanoSIMS mu m-scale *in situ* measurement of C-13/C-12 in early Precambrian organic matter, with permil precision. *International Journal of Mass Spectrometry* **278**, 59–68.

French KL, Hallmann C, Hope JM, Schoon PL, Zumberge JA, Hoshino Y, Peters CA, George SA, Love GD, Brocks JJ, Buick R, Summons RE (2015) Reappraisal of hydrocarbon biomarkers in Archean rocks. *Proceedings of the National Academy of Sciences of the United States of America*, **112**, 5915–5920.

Guo QJ, Strauss H, Kaufman AJ, Schroder S, Gutzmer J, Wing B, Baker MA, Bekker A, Jin QS, Kim ST, Farquhar J (2009) Reconstructing Earth's surface oxidation across the Archean-Proterozoic transition. *Geology* **37**, 399–402.

Hassler SW, Simonson BM, Sumner DY, Murphy M (2005) Neoarchaean impact spherule layers in the Fortescue and Hamersley Groups, Western Australia: stratigraphic and depositional implications of re-correlation. *Australian Journal of Earth Sciences* **52**, 759–771.

Hayes JM (1983) Geochemical evidence bearing on the origin of aerobiosis, a speculative hypothesis. In *Earth's Earliest Biosphere: Its Origin and Evolution*. (ed. Schopf JW). Princeton University Press, Princeton, pp. 291–301.

Hayes JM (1994) Global methanotrophy at the Archean-Proterozoic transition. In: *Early Life on Earth, Nobel Symposium No. 84* (ed. Bengtson S). Columbia University Press, New York, pp. 220–236.

Johnson JE, Webb SM, Thomas K, Ono S, Kirschvink JL, Fischer WW (2013) Manganese-oxidizing photosynthesis before the rise of cyanobacteria. *Proceedings of the National Academy of Sciences of the United States of America* **110**, 11238–11243.

Johnston DT (2011) Multiple sulfur isotopes and the evolution of Earth's surface sulfur cycle. *Earth-Science Reviews* **106**, 161–183.

Johnston DT, Farquhar J, Wing BA, Lyons T, Kah L, Strauss H, Canfield DE (2005) Using the multiple isotopes of sulfur to constrain microbial processes in the Proterozoic ocean. *Geochimica Et Cosmochimica Acta* **69**, A548–A548.

Johnston DT, Farquhar J, Canfield DE (2007) Sulfur isotope insights into microbial sulfate reduction: when microbes meet models. *Geochimica Et Cosmochimica Acta* **71**, 3929–3947.

Johnston DT, Farquhar J, Habicht KS, Canfield DE (2008) Sulphur isotopes and the search for life: strategies for identifying sulphur metabolisms in the rock record and beyond. *Geobiology* **6**, 425–435.

Kakegawa T, Nanri H (2006) Sulfur and carbon isotope analyses of 2.7 Ga stromatolites, cherts and sandstones in the Jeerinah Formation. *Western Australia. Precambrian Research* **148**, 115–124.

Kakegawa T, Kasahara Y, Hayashi K, Ohmoto H (2000) Sulfur and carbon isotope analyses of the 2.7 Ga Jeerinah Formation, Fortescue Group, Australia. *Geochemical Journal* **34**, 121–133.

Kaufman AJ, Johnston DT, Farquhar J, Masterson AL, Lyons TW, Bates S, Anbar AD, Arnold GL, Garvin J, Buick R (2007) Late Archean biospheric oxygenation and atmospheric evolution. *Science* **317**, 1900–1903.

Kita NT, Ushikubo T, Fu B, Valley JW (2009) High precision SIMS oxygen isotope analysis and the effect of sample topography. *Chemical Geology* **264**, 43–57.

Kita NT, Sobol PE, Kern JR, Lord NE, Valley JW (2015) UV light microscope: improvements in optical imaging for a secondary ion mass spectrometer. *Journal of Analytical Atomic Spectrometry* **30**, 1207–1213.

Kitchen NE, Valley JW (1995) Carbon-isotope thermometry in marbles of the Adirondack mountains, New York. *Journal of Metamorphic Geology* **13**, 577–594.

Kozdon R, Ushikubo T, Kita NT, Spicuzza M, Valley JW (2009) Intratest oxygen isotope variability in the planktonic foraminifer N. pachyderma: real vs. apparent vital effects by ion microprobe. *Chemical Geology* **258**, 327–337.

Kozdon R, Kita NT, Huberty JM, Fournelle JH, Johnson CA, Valley JW (2010) *In situ* sulfur isotope analysis of sulfide minerals by SIMS: precision and accuracy, with application to thermometry of similar to 3.5 Ga Pilbara cherts. *Chemical Geology* **275**, 243–253.

Landais P, Dubessy J, Dereppe JM, Philp RP (1993) Characterization of graphite alteration and bitumen genesis in the Cigar Lake deposit (Saskatchewan, Canada). *Canadian Journal of Earth Sciences* **30**, 743–753.

Lasaga AC, Otake T, Watanabe Y, Ohmoto H (2008) Anomalous fractionation of sulfur isotopes during heterogeneous reactions. *Earth and Planetary Science Letters* **268**, 225–238.

Lepot K, Benzerara K, Rividi N, Cotte M, Brown GE, Philippot P (2009) Organic matter heterogeneities in 2.72 Ga stromatolites: alteration versus preservation by sulfur incorporation. *Geochimica Et Cosmochimica Acta* **73**, 6579–6599.

Lepot K, Williford KH, Ushikubo T, Sugitani K, Mimura K, Spicuzza MJ, Valley JW (2013) Biogenicity of 3.4 Gyr old carbon indicated by texture-specific isotopic compositions. *Nature Geoscience* **112**, 66–86.

Marin-Carbonne J, Rollion-Bard C, Bekker A, Rouxel O, Agangi A, Cavalazzi B, Wohlgemuth-Ueberwasser CC, Hofmann A, Mckeegan KD (2014) Coupled Fe and S isotope variations in pyrite nodules from Archean shale. *Earth and Planetary Science Letters* **392**, 67–79.

Oehler DZ, Robert F, Walter MR, Sugitani K, Allwood A, Meibom A, Mostefaoui S, Selo M, Thomen A, Gibson EK (2009) NanoSIMS: insights to biogenicity and syngeneity of Archaean carbonaceous structures. *Precambrian Research* **173**, 70–78.

Ono S (2008) Multiple-sulphur isotope biosignatures. *Space Science Reviews* **135**, 203–220.

Ono S, Eigenbrode JL, Pavlov AA, Kharecha P, Rumble D, Kasting JF, Freeman KH (2003) New insights into Archean sulfur cycle from mass-independent sulfur isotope records from the Hamersley Basin, Australia. *Earth and Planetary Science Letters* **213**, 15–30.

Ono S, Wing B, Johnston D, Farquhar J, Rumble D (2006) Mass-dependent fractionation of quadruple stable sulfur isotope system as a new tracer of sulfur biogeochemical cycles. *Geochimica Et Cosmochimica Acta* **70**, 2238–2252.

Orphan VJ, House CH (2009) Geobiological investigations using secondary ion mass spectrometry: microanalysis of extant and paleo-microbial processes. *Geobiology* **7**, 360–372.

Orphan VJ, Hinrichs KU, Ussler W, Paull CK, Taylor LT, Sylva SP, Hayes JM, Delong EF (2001a) Comparative analysis of methane-oxidizing archaea and sulfate-reducing bacteria in anoxic marine sediments. *Applied and Environmental Microbiology* **67**, 1922–1934.

Orphan VJ, House CH, Hinrichs KU, Mckeegan KD, Delong EF (2001b) Methane-consuming archaea revealed by directly coupled isotopic and phylogenetic analysis. *Science* **293**, 484–487.

Papineau D, Mojzsis SJ, Schmitt AK (2007) Multiple sulfur isotopes from Paleoproterozoic Huronian interglacial sediments and the rise of atmospheric oxygen. *Earth and Planetary Science Letters* **255**, 188–212.

Pappano PJ (2001) *Graphitization studies of Pennsylvania anthracites. M.S. Thesis.* The Pennsylvania State University, University Park, PA, USA.

Pavlov AA, Kasting JF (2002) Mass-independent fractionation of sulfur isotopes in Archean sediments: strong evidence for an anoxic Archean atmosphere. *Astrobiology* **2**, 27–41.

Philippot P, Van Zuilen M, Lepot K, Thomazo C, Farquhar J, Van Kranendonk MJ (2007) Early Archaean microorganisms preferred elemental sulfur, not sulfate. *Science* **317**, 1534–1537.

Philippot P, Van Zuilen M, Rollion-Bard C (2012) Variations in atmospheric sulphur chemistry on early Earth linked to volcanic activity. *Nature Geoscience* **5**, 668–U100.

Pufahl PK, Hiatt EE, Kyser TK (2010) Does the Paleoproterozoic Animikie Basin record the sulfidic ocean transition? *Geology* **38**, 659–662.

Rasmussen B (2005) Evidence for pervasive petroleum generation and migration in 3.2 and 2.63 Ga shales. *Geology* **33**, 497–500.

Rasmussen B, Fletcher IR, Sheppard S (2005) Isotopic dating of the migration of a low-grade metamorphic front during orogenesis. *Geology* **33**, 773–776.

Rasmussen B, Fletcher IR, Brocks JJ, Kilburn MR (2008) Reassessing the first appearance of eukaryotes and cyanobacteria. *Nature* **455**, 1101–U1109.

Sangély L, Chaussidon M, Michels R, Huault V (2005) Microanalysis of carbon isotope composition in organic matter by secondary ion mass spectrometry. *Chemical Geology* **223**, 179–195.

Sangély L, Chaussidon M, Michels R, Brouand M, Cuney M, Huault V, Landais P (2007) Micrometer scale carbon isotopic study of bitumen associated with Athabasca uranium deposits: constraints on the genetic relationship with petroleum source-rocks and the abiogenic origin hypothesis. *Earth and Planetary Science Letters* **258**, 378–396.

Shen Y, Buick R, Canfield DE (2001) Isotopic evidence for microbial sulphate reduction in the early Archaean era. *Nature* **410**, 77–81.

Shen Y, Farquhar J, Masterson A, Kaufman AJ, Buick R (2009) Evaluating the role of microbial sulfate reduction in the early Archean using quadruple isotope systematics. *Earth and Planetary Science Letters* **279**, 383–391.

Sheppard SM, Schwarcz HP (1970) Fractionation of carbon and oxygen isotopes and magnesium between coexisting metamorphic calcite and dolomite. *Contributions to Mineralogy and Petrology* **26**, 161–198.

Shields G, Veizer J (2002) Precambrian marine carbonate isotope database: version 1.1. *Geochemistry Geophysics Geosystems*, **3** doi:10.1029/2001GC000266.

Slodzian G, Hillion F, Stadermann FJ, Zinner E (2004) QSA influences on isotopic ratio measurements. *Applied Surface Science* **231**, 874–877.

Smith RE, Perdrix JL, Parks TC (1982) Burial metamorphism in the Hamersley Basin, Western Australia. *Journal of Petrology* **23**, 75–102.

Thomazo C, Ader M, Farquhar J, Philippot P (2009a) Methanotrophs regulated atmospheric sulfur isotope anomalies during the Mesoarchean (Tumbiana Formation, Western Australia). *Earth and Planetary Science Letters* **279**, 65–75.

Thomazo C, Pinti DL, Busigny V, Ader M, Hashizume K, Philippot P (2009b) Biological activity and the Earth's surface evolution: insights from carbon, sulfur, nitrogen and iron stable isotopes in the rock record. *Comptes Rendus Palevol* **8**, 665–678.

Thomazo C, Nisbet EG, Grassineau NV, Peters M, Strauss H (2013) Multiple sulfur and carbon isotope composition of sediments from the Belingwe Greenstone Belt (Zimbabwe): a biogenic methane regulation on mass independent fractionation of sulfur during the Neoarchean? *Geochimica Et Cosmochimica Acta* **121**, 120–138.

Trendall AF, Blockley JG (1970) The iron formations of the Precambrian Hamersley Group, Western Australia. *Geological Survey of Western Australia: Bulletin*, **119**, 366.

Tyler SA, Barghoorn ES, Barrett LP (1957) Anthracitic coal from Precambrian Upper Huronian Black Shale of the Iron River District, Northern Michigan. *Geological Society of America Bulletin* **68**, 1293–1304.

Ushikubo T, Williford KH, Farquhar J, Johnston DT, Van Kranendonk MJ, Valley JW (2014) Development of in situ sulfur four-isotope analysis with multiple Faraday cup detectors by SIMS and application to pyrite grains in a Paleoproterozoic glaciogenic sandstone. *Chemical Geology* **383**, 86–99.

Valley JW, Kita NT (2009) *In situ* Oxygen Isotope Geochemistry by Ion Microprobe. In: *MAC Short Course: Secondary Ion Mass Spectrometry in the Earth Sciences* (ed. Fayek M). Mineralogical Association of Canada, Québec, Canada, pp. 19–63.

Veizer J, Clayton RN, Hinton RW, Vonbrunn V, Mason TR, Buck SG, Hoefs J (1990) Geochemistry of Precambrian carbonates: 3 - shelf seas and nonmarine environments of the Archean. *Geochimica Et Cosmochimica Acta* **54**, 2717–2729.

Wacey D, Gleeson D, Kilburn MR (2010) Microbialite taphonomy and biogenicity: new insights from NanoSIMS. *Geobiology* **8**, 403–416.

Waldbauer JR, Sherman LS, Sumner DY, Summons RE (2009) Late Archean molecular fossils from the Transvaal Supergroup record the antiquity of microbial diversity and aerobiosis. *Precambrian Research* **169**, 28–47.

Watanabe Y, Farquhar J, Ohmoto H (2009) Anomalous Fractionations of Sulfur Isotopes During Thermochemical Sulfate Reduction. *Science* **324**, 370–373.

White AJR, Legras M, Smith RE, Nadoll P (2014a) Deformation-driven, regional-scale metasomatism in the Hamersley Basin, Western Australia. *Journal of Metamorphic Geology* **32**, 417–433.

White AJR, Smith RE, Nadoll P, Legras M (2014b) Regional-scale metasomatism in the fortescue group volcanics, Hamersley Basin, Western Australia: implications for hydrothermal ore systems. *Journal of Petrology* **55**, 977–1009.

Williford KH, Van Kranendonk MJ, Ushikubo T, Kozdon R, Valley JW (2011) Constraining atmospheric oxygen and seawater sulfate concentrations during Paleoproterozoic glaciation: *In situ* sulfur three-isotope microanalysis of pyrite from the Turee Creek Group, Western Australia. *Geochimica Et Cosmochimica Acta* **75**, 5686–5705.

Williford KH, Ushikubo T, Schopf JW, Lepot K, Kitajima K, Valley JW (2013) Preservation and detection of microstructural and taxonomic correlations in the carbon isotopic compositions of individual Precambrian microfossils. *Geochimica Et Cosmochimica Acta* **104**, 165–182.

Yamaguchi KE (2002) Geochemistry of Archean-Paleoproterozoic black shales: the early evolution of the atmosphere, oceans, and biosphere. PhD dissertation, Pennsylvania State University.

Yamaguchi KE, Johnson CM, Beard BL, Ohmoto H (2005) Biogeochemical cycling of iron in the Archean-Paleoproterozoic Earth: constraints from iron isotope variations in sedimentary rocks from the Kaapvaal and Pilbara Cratons. *Chemical Geology* **218**, 135–169.

Zerkle AL, Kamyshny A, Kump LR, Farquhar J, Oduro H, Arthur MA (2010) Sulfur cycling in a stratified euxinic lake with moderately high sulfate: constraints from quadruple S isotopes. *Geochimica Et Cosmochimica Acta* **74**, 4953–4970.

Zerkle AL, Claire M, Domagal-Goldman SD, Farquhar J, Poulton SW (2012) A bistable organic-rich atmosphere on the Neoarchaean Earth. *Nature Geoscience* **5**, 359–363.

Zhelezinskaia I, Kaufman AJ, Farquhar J, Cliff J (2014) Large sulfur isotope fractionations associated with Neoarchean microbial sulfate reduction. *Science* **346**, 742–744.

SUPPORTING INFORMATION

Additional Supporting Information may be found in the online version of this article:

Data S1. Supplementary materials.